

Search for gravitational lens system candidates at milli-arcsecond scales using EVN data at 5 and 22 GHz

by

George Kalaitzidakis

Supervisor: Carolina Casadio

Bachelor Thesis



UNIVERSITY OF CRETE

Department of Physics

May 2023

Abstract

The principal aim of the work presented in this thesis is the verification of strong gravitational lens candidates within a catalogue of compact radio sources. This study is part of the Search for Milli-LEnses (SMILE) project, focused on the search for gravitational lens systems on milliarcsecond scales, using Very Long Baseline Interferometry (VLBI) data at radio frequencies. In the work presented here, we initially selected milli-lens candidates from the publicly available Astrogéo database, and we observed them with the European VLBI Network (EVN) at 5 and 22 GHz. We obtained the radio images of these sources and analyzed a number of physical quantities that we expect to help us judge whether a source is a gravitational lens system or not. Out of the 16 sources that were studied in this work, 3 passed all tests and are still considered as valid candidates. Additional follow-up studies are needed to prove whether they are indeed gravitational lens systems.

Contents

| | |
|---|------------|
| Abstract | i |
| List of Figures | iii |
| List of Tables | v |
| Abbreviations | vi |
| 1 Introduction | 1 |
| 2 The Physics of Active Galactic Nuclei | 4 |
| 3 The Pilot Search for Milli-lenses | 9 |
| 4 EVN follow-up study of milli-lens candidates | 12 |
| 4.1 Very Long Baseline Interferometry data | 13 |
| 4.2 Phase and amplitude calibration | 15 |
| 4.3 Imaging and self-calibration | 16 |
| 4.4 Model Fitting | 18 |
| 4.5 Data Analysis | 18 |
| 5 Results | 23 |
| 5.1 J0213+8717 | 24 |
| 5.2 J0237+1116 | 25 |
| 5.3 J0455-2034 | 26 |
| 5.4 J0527+1743 | 28 |
| 5.5 J0602-2546 | 29 |
| 5.6 J0616-1957 | 30 |
| 5.7 J0729-1320 | 31 |
| 5.8 J0732+6023 | 32 |
| 5.9 J0840-0648 | 33 |
| 5.10 J0900-0652 | 34 |
| 5.11 J0918+2650 | 35 |
| 5.12 J1037+4335 | 36 |
| 5.13 J1132+5100 | 37 |
| 5.14 J1143+1834 | 38 |
| 5.15 J1306+0341 | 40 |
| 5.16 J1344-1739 | 41 |
| 6 Conclusion | 42 |
| Bibliography | 43 |

List of Figures

| | | |
|------|---|----|
| 1.1 | The SMILE: Search for Milli-LEnses project website | 3 |
| 2.1 | The spectral energy distribution of the blazar Markarian 421 | 5 |
| 2.2 | The synchrotron radiation spectrum of a single electron shown with a) linear and b) logarithmic axes | 6 |
| 2.3 | The radiation spectrum of a partially self-absorbed synchrotron source | 7 |
| 3.1 | The web page for the visual inspection of sources used in the pilot study | 10 |
| 4.1 | The uv plot of J1037+4335 during the epoch 26/02/2020 observed at 4.926 GHz | 15 |
| 4.2 | The final residual map of J0527+1743 | 17 |
| 4.3 | The clean map of J0527+1743 | 17 |
| 5.1 | J0213+8717 EVN 5 GHz data | 24 |
| 5.2 | J0213+8717 Astrogeo data at 2.3 GHz (S-band) and 8 GHz (X-band) | 24 |
| 5.3 | J0237+1116 EVN 5 GHz data | 25 |
| 5.4 | J0237+1116 Astrogeo data at 4.3 GHz (C-band) and 8 GHz (X-band) | 25 |
| 5.5 | J0455-2034 EVN 5 GHz data | 26 |
| 5.6 | J0455-2034 2010/12/21 Astrogeo data at 8 GHz (X-band) | 27 |
| 5.7 | J0455-2034 2011/01/13 Astrogeo data at 8 GHz (X-band) | 27 |
| 5.8 | J0527+1743 EVN 5 GHz data | 28 |
| 5.9 | J0527+1743 Astrogeo data at 4.3 GHz (C-band) and 8 GHz (X-band) | 28 |
| 5.10 | J0602-2546 EVN 5 GHz data | 29 |
| 5.11 | J0602-2546 Astrogeo data at 4.3 GHz (C-band) and 8 GHz (X-band) | 29 |
| 5.12 | J0616-1957 EVN 5 GHz data | 30 |
| 5.13 | J0616-1957 Astrogeo data at 4.3 GHz (C-band) and 8 GHz (X-band) | 30 |
| 5.14 | J0729-1320 EVN 5 GHz data | 31 |
| 5.15 | J0729-1320 Astrogeo data at 2.3 GHz (S-band) and 8 GHz (X-band) | 31 |
| 5.16 | J0732+6023 EVN 5 GHz data | 32 |
| 5.17 | J0732+6023 Astrogeo data at 4.3 GHz (C-band) and 8 GHz (X-band) | 32 |
| 5.18 | J0840-0648 EVN 5 GHz data | 33 |
| 5.19 | J0840-0648 Astrogeo data at 4.3 GHz (C-band) and 8 GHz (X-band) | 33 |
| 5.20 | J0900-0652 EVN 5 GHz data | 34 |
| 5.21 | J0900-0652 Astrogeo data at 4.3 GHz (C-band) and 8 GHz (X-band) | 34 |
| 5.22 | J0918+2650 EVN 5 GHz data | 35 |
| 5.23 | J0918+2650 Astrogeo data at 4.3 GHz (C-band) and 8 GHz (X-band) | 35 |
| 5.24 | J1037+4335 EVN 5 GHz data | 36 |
| 5.25 | J1037+4335 Astrogeo data at 8 GHz (X-band) | 36 |
| 5.26 | J1132+5100 EVN 5 GHz data | 37 |
| 5.27 | J1132+5100 Astrogeo data at 4.3 GHz (C-band) and 8 GHz (X-band) | 37 |

| | | |
|------|---|----|
| 5.28 | J1143+1834 EVN 5 GHz data | 38 |
| 5.29 | J1143+1834 Astrogeo data at 2.3 GHz (S- band), 4.3 GHz (C-band), 8 GHz (X- band) and 15.1 GHz (U-band) | 38 |
| 5.30 | J1143+1834 EVN 22 GHz data | 38 |
| 5.31 | J1306+0341 EVN 5 GHz data | 40 |
| 5.32 | J1306+0341 Astrogeo data at 4.3 GHz (C-band) and 8 GHz (X-band) | 40 |
| 5.33 | J1344-1739 EVN 5 GHz data | 41 |
| 5.34 | J1344-1739 Astrogeo data at 4.3 GHz (C-band) and 8 GHz (X-band) | 41 |

List of Tables

| | | |
|------|--|----|
| 4.1 | Sources included in the 40 best lens candidates from the Astrogeo database . . . | 12 |
| 5.1 | J0213+8717 | 24 |
| 5.2 | J0237+1116 | 26 |
| 5.3 | J0527+1743 | 28 |
| 5.4 | J0602-2546 | 29 |
| 5.5 | J0616-1957 | 30 |
| 5.6 | J0729-1320 | 31 |
| 5.7 | J0732+6023 | 32 |
| 5.8 | J0840-0648 | 33 |
| 5.9 | J0900-0652 | 34 |
| 5.10 | J0918+2650 | 35 |
| 5.11 | J1132+5100 | 37 |
| 5.12 | J1143+1834 | 39 |
| 5.13 | J1306+0341 | 40 |
| 5.14 | J1344-1739 | 41 |

Abbreviations

| | |
|--------------------------------|---|
| AGN | A ctive G alactic N ucleus |
| (C/W)DM | (C old/ W arm) D ark M atter |
| SBBH | S upermassive B inary B lack H ole |
| CSO | C ompact S ymmetric O bject |
| EVN | E uropean VLBI N etwork |
| FR | F lux R atio |
| FWHM | F ull W idth at H alf M aximum |
| RMS | R oot M ean S quare |
| SB | S urface B rightness |
| SMCO | S uper M assive C ompact O bject |
| VLBI | V ery L ong B aseline I nterferometry |
| ΛCDM | L ambda C old D ark M atter |

Chapter 1

Introduction

Dark Matter (DM), still to this day, poses a great challenge for scientists who want to understand its nature and characteristics. Along with dark energy, they make up for the vast majority of the energy density of the universe (approximately 95%), but, despite that, they remain mysterious and have baffled scientists for decades. Nowadays, the cosmological model used to explain the structure formation and evolution in our universe is the Lambda Cold Dark Matter (Λ CDM) model, according to which approximately 23% of the mass-energy content of the universe corresponds to DM. Lambda is the cosmological constant associated with dark energy, while *cold dark matter* (CMD) refers to the most popular type of DM currently theorized. The term "cold" refers to the assumption that the particles' speed is quite small compared to the speed of light. In general this model has displayed considerable success in its predictions for large-scale structures (Del Popolo 2002). Nonetheless Λ CDM has difficulty in predicting the currently observed number of structures at smaller sub-galactic scales, i.e. masses below $10^{11} M_{\odot}$ (Popolo & Delliou 2017; Weinberg et al. 2015). Moreover, at sub-galactic scales different DM models make very different predictions. For example, the *warm dark matter* (WDM) model, as opposed to CDM, predicts the formation of a smaller number of low mass haloes. This is because, according to this model, the initial velocities of WDM particles were considerably dispersed. The free streaming of these particles led to the smoothing of the dark matter distribution, preventing the formation of sub-galactic haloes. (Paduroiu et al. 2015; Viel et al. 2005). Differences like this are of major significance if we want to find experimental ways to distinguish between the different models and figure out which one comes closer in describing the universe we actually observe.

Generally, DM particles do not seem to interact with the electromagnetic field, making their direct observation impossible. The only way to observe them is through the gravitational effects they exert on ordinary matter. DM halos with sub-galactic masses like the ones we are looking for are expected to have a substantial mass concentration, at least at their centers, to create a phenomenon called *strong gravitational lensing* (Vegetti et al. 2012; Hezaveh et al. 2016). Gravitational lensing is the physical phenomenon that takes place when the light from a distant source passes near an object with great mass concentration (the *lens*), resulting in its trajectory getting bent. In specific cases where, according to the observer, the source is behind the lens and the lens has a surface mass density greater than a critical value, we observe the phenomenon of strong gravitational lensing, where an observer on earth could detect multiple images of the same luminous source in background form. The scale of the angular separation between the different observed lensed images can also reveal a lot about the nature of the lens. This study focuses on sources with angular separation of the order of milli-arcseconds that is believed to correspond to supermassive compact objects with masses in the range $\sim 10^6 - 10^9 M_\odot$. A search for milli-lenses can then provide information on the abundance of supermassive compact objects in the Universe, and help us to discriminate between different DM models, as described in Loudas et al. (2022). Besides the aforementioned DM halos we are searching for, these lenses could account for supermassive compact objects like primordial black holes away from galaxies, that also constitute a possible DM candidate, or black holes, like the ones located in the nucleus of active galaxies. Despite the existence of objects like Bright and Classical Dwarf galaxies with stellar masses in the mass range of our interest (Bullock & Boylan-Kolchin 2017), no gravitational lens systems have been discovered at milli-arcsecond scales yet.

This work is part of the SMILE: Search for Milli-LEnses project and is a continuation of a pilot project that was carried out in 2020. The official webpage of the project can be found at <https://smilescience.info> (Figure 1.1). The principal goal of the SMILE project is the search and possible discovery of gravitational lens system candidates at milli-arcsecond scales (also referred to as milli-lenses), using high resolution VLBI data. The focus of this work in particular is on radio VLBI observations at 5 GHz performed with the EVN, while also including and taking into account older data and results from the pilot project. Any confirmed lens candidate will be investigated with further multi-frequency follow-up observations and, ultimately, tested against a gravitational lens model. The discovery of a milli-lens system would be a major discovery, as no gravitational lens system at these mass scales has been found yet, but even a null result would

lead to important conclusions (Loudas et al. 2022). Even if no lens candidates are discovered, this fact by itself can be of major importance in constraining the abundance of supermassive compact objects (SMCOs) in the universe with much better precision than in previous studies (Wilkinson et al. 2001).



Search for Milli-LEnses to discriminate between dark matter models

HOME

TEAM

JOBS

With the SMILE project we propose to search for gravitational lens systems on milli-arcsecond scales, i.e. milli-lenses, using a large (~5000 sources) and complete sample of radio loud active galaxies and high resolution Very Long Baseline Interferometry (VLBI) data. Gravitational lensed images with angular separation on milliarcsecond scales probe gravitational lens systems where the lens is a supermassive compact object, i.e. a compact object with mass in the range $10^6 - 10^7 M_\odot$. This mass range is particularly critical for the widely accepted Λ Cold Dark Matter (Λ CDM) model, which predicts many more dark matter (DM) halos at sub-galactic scales ($<10'' M_\odot$), than currently observed.

Since the number of DM sub-galactic halos that can be detected through milli-lenses depends both on the mass function and the density profiles of DM halos, with the SMILE project we will be able to discriminate between many currently viable DM models. Milli-lensing is not only sensitive to DM halos at sub-galactic scales, but also at (i) primordial black holes, also considered an alternative candidate to DM particles, and (ii) supermassive black holes hosted by galaxies.

In Casadio et al., 2021, MNRAS, 507, L6 we presented a pilot search for milli-lenses with angular separation smaller than 150 milli-arcseconds, using the publicly available multi-frequency VLBI data in the *Astropo-VLBI FITS Image database*. We identified 40 new milli-lens candidates, and obtained new follow-up observations with the European VLBI Network (EVN).

In order to reach our goal, we will develop advanced and automatized VLBI data reduction techniques and we will deliver to the community high quality VLBI images of an unprecedented number of sources. Sources that will be finally rejected as milli-lens systems can still be investigated as binary supermassive black holes or compact symmetric objects candidates. In both cases, we are talking about intriguing and poorly understood objects, which will deserve dedicated studies and publications.

SMILE project has received funding from the European Research Council (ERC) under the HORIZON ERC Grants 2021 programme (grant agreement No 101040021)

© Search for Milli-Lenses (SMILE) project

When our line of sight to radio-loud quasars intersects a supermassive compact object, like a dark matter clump, a double image may form via the effect of gravitational lensing. Within the SMILE project we will systematically look for such double images, which can reveal the nature of dark matter.

FIGURE 1.1: The SMILE: Search for Milli-LEnses project website

Chapter 2

The Physics of Active Galactic Nuclei

Most of the sources considered in this study are radio loud active galaxies. With the term "active" we refer to galaxies that host a supermassive black hole (with a mass from $\sim 10^6$ to $\sim 10^9 M_\odot$) in their centre and show signs of nuclear activity. This often includes the presence of outflows in the form of very bright jets. These immensely luminous objects are called *active galactic nuclei* (AGN). A brief overview of their radiative processes and spectra is important if we want to be able to differentiate between the image of a lensed background source and that of the core and jet of an AGN.

The most luminous class of AGN are *blazars*. What differentiates them from other types of AGN is the direction of their jet that is very close to our line of sight, making them particularly bright. According to the current models, the emission mechanism of such objects is not thermal, but rather mainly synchrotron and inverse Compton radiation. In Figure 2.1 we present an example of the characteristic spectral energy distribution of a blazar from [Abdo et al. \(2011\)](#).

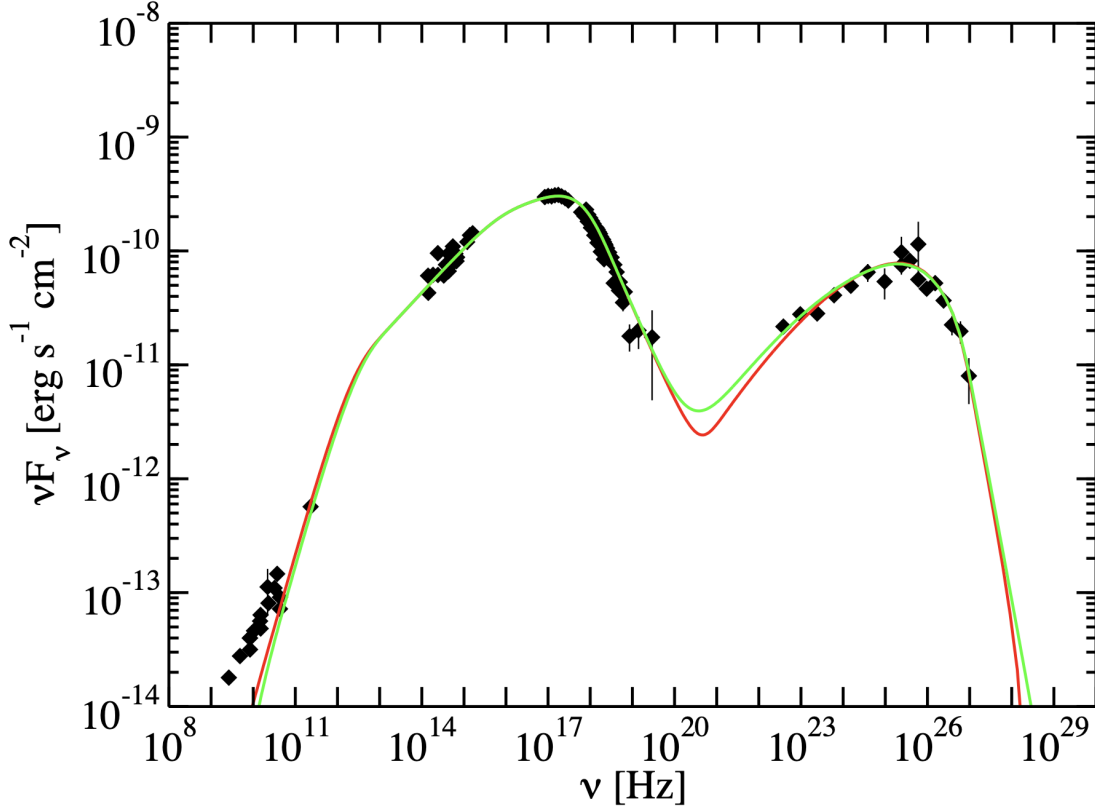


FIGURE 2.1: The spectral energy distribution of the blazar Markarian 421

The low energy peak, from radio to UV or X-ray frequencies, is associated with synchrotron emission from the relativistic electrons forming jets, and the high energy peak is associated with inverse Compton scattering of the same electron population. The emission originating from jets is influenced by effects such as relativistic beaming, stemming from the fact that these electrons are moving with velocities close to the speed of light. We can use the Larmor formula $P = \frac{2}{3} \frac{q^2}{c^3} a^2$, where q is the charge and a the acceleration of a particle, to show that the total radiated power in the synchrotron process is given by equation 2.1, as presented in Casadio (2016):

$$P_s = \frac{2}{3} \frac{e^4}{m_e^2 c^3} \left(\frac{E}{m_e c^2} \right)^2 B^2 \sin^2 \phi \quad (2.1)$$

Here m_e is the electron mass and ϕ is the angle between the velocity of the particle and the magnetic field. We observe a dependence of the radiated power on the squares of both the electron energy E and the magnetic field B . The characteristic synchrotron spectrum for a single electron has the form displayed in Figure 2.2, as presented in Longair (2011).

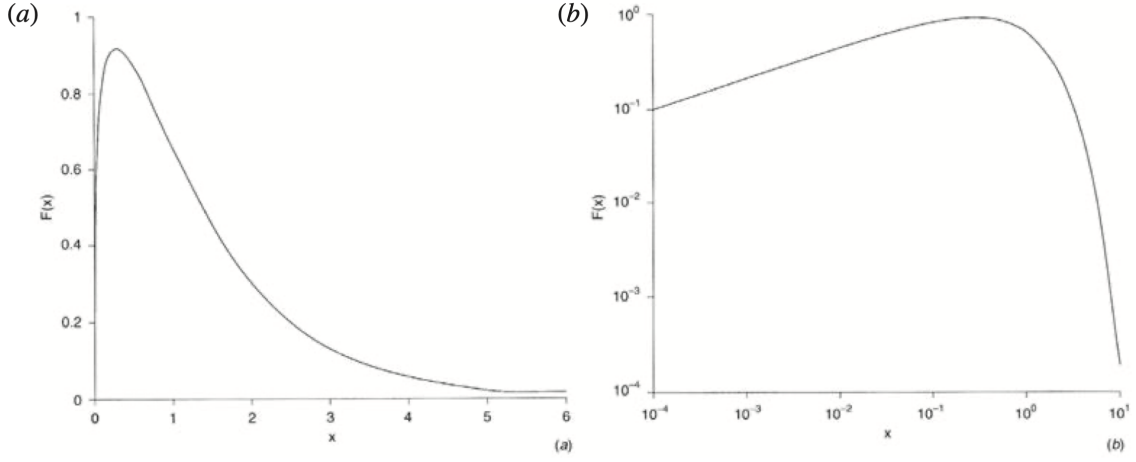


FIGURE 2.2: The synchrotron radiation spectrum of a single electron shown with a) linear and b) logarithmic axes

For the radiation spectrum of the whole structure we need to account for the total contribution of all electrons, obtaining that the relation between the flux density F of the source and the frequency ν is described by a power law of the general form:

$$F \propto \nu^\alpha \quad (2.2)$$

where α is the *spectral index* and, in the case of synchrotron emission, is expected to have a negative value. Additionally, we can account for processes like the synchrotron self-absorption at lower frequencies and radiation losses at higher frequencies. The latter is due to the high energy electrons that emit substantially more energy as can be seen in equation 2.1. The theoretical synchrotron radiation spectrum after these adjustments has the form presented in Figure 2.3.

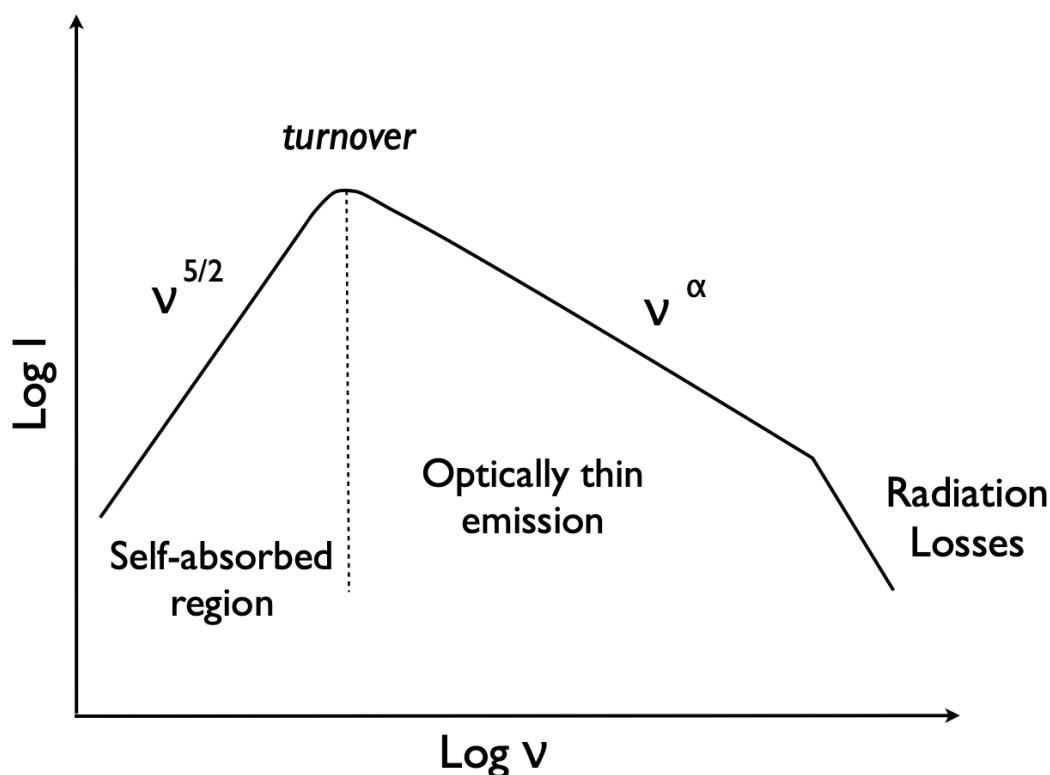


FIGURE 2.3: The radiation spectrum of a partially self-absorbed synchrotron source

Another notable characteristic of radio observations of AGN is that they usually display structures consisting of multiple distinct components. The more compact, brightest component corresponds to the *core* of the jet and is thought to be the region at which the transition between optically thick and thin emission takes place (Konigl 1981). Such a scenario predicts a displacement of the core towards the central engine of the AGN for higher frequency observations. This is found to not be true for all observed sources, thus indicating that the core could be a "recollimation" shock farther downstream caused by the interaction of the jet with ambient features (Marscher 2008; Gomez et al. 1995). It should be noted that the core in VLBI images of such objects is usually not equivalent to the base of the jet itself. Moreover, it is characterised by a flat spectrum. A secondary bright component observed in VLBI images could then correspond to a perturbation along the jet (*knot*) or a stationary feature like a recollimation shock. This component is expected to have a much steeper spectrum than the core.

Two additional types of radio-emitting AGN that can mimic the shape of a gravitational lens at these wavelengths are *Compact Symmetric Objects* (CSO) and *Supermassive Binary Black Hole*

(SBBH) systems. CSOs are much smaller in comparison to the aforementioned radio-loud AGN and display a symmetric double-lobe structure around a central core. They were believed to be the first evolutionary stages of symmetric jetted AGN ([Frey et al. 2022](#)), but new studies suggest that they could be an entirely separate class of jetted AGN ([Kiehlmann et al. 2023a,b](#); [Readhead et al. 2023](#)). A similar double-component structure is expected in a SBBH system because of the existence of emission originating from the black hole pair in galaxy mergers ([Taylor et al. 2006](#); [Voggel et al. 2022](#)). Both CSOs and SBBHs constitute alternative candidates for a number of the sources presented in the study.

Chapter 3

The Pilot Search for Milli-lenses

Using publicly available multi-frequency, multi-epoch VLBI data from the Astrogeo VLBI FITS image database (<http://astrogeo.org/>), we collected data for 13,828 different objects and we combined, by averaging, multi-epoch observations that were obtained for the same object and at the same frequency.

A web page was created for the visualization of images by multiple users. There, the final images of the sources were displayed in all the available frequency bands and covering a field of view of $300 \times 300 \text{ mas}^2$, centered at the source coordinates (Figure 3.1). Most sources had two available frequency bands, between the X-band (7.6–8.5 GHz), C-band (4.3–5.0 GHz) and S-band (2.2–2.3 GHz). In some rare cases, like with the source J1143+1834, we had observations in all three of them. The web page also allowed the user to change parameters like the flux density levels, the dynamic range or the zoom of each image for a better inspection.

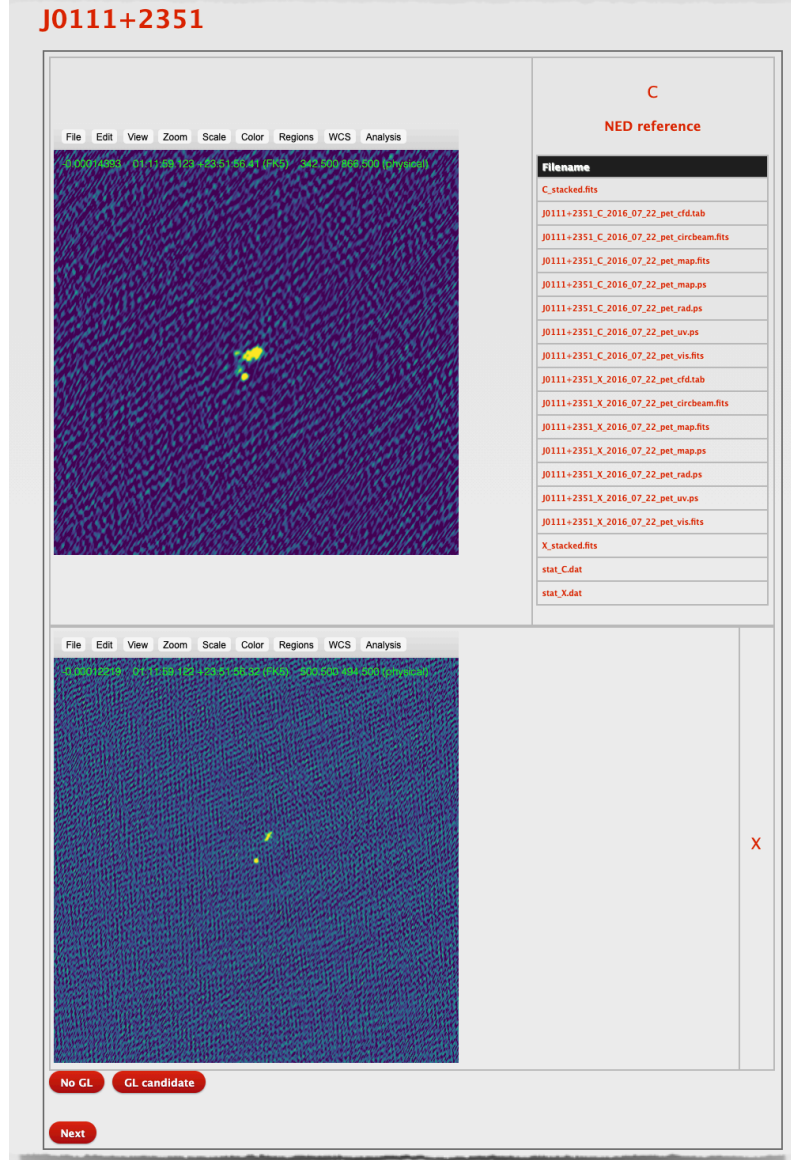


FIGURE 3.1: The web page for the visual inspection of sources used in the pilot study

The search was carried out by a team consisting of 5 PhD scientists and 9 undergraduate students from the Physics Department of the University of Crete. We were assigned the task to go through a number of randomly selected sources and visually inspect them. We then had to classify them according to whether they were possible gravitational lens system candidates or not. The main criterion for this choice was the number of visible components. If a source, in any of the displayed images, was showing two or more compact components in any of the available bands, it was catalogued as a lens candidate. In order to ensure the highest possible accuracy, and avoid human errors, a number of artificial sources were inserted among the real ones, making it

easier to judge and correct potential oversights and mistakes. From this process 954 sources were categorised as lens candidates in total, with an estimate of the total loss rate close to 1%.

Afterwards, the 954 sources were visually inspected again by some of the researchers involved in the project. This time they paid attention to the surface brightness (SB) and the spectra of the supposed lensed images, since these two quantities are expected to be preserved in gravitational lensing. Moreover, sources that showed characteristics like obvious processing artifacts or just a core-jet structure were discarded from our remaining pool. After these multiple steps of visual inspections, the selected lens candidates were 59 in total. Ultimately, we computed the SB of all putative lensed images and discarded sources with a SB ratio between components >7 . The list of the 40 best milli-lens candidates that passed this final test was published in [Casadio et al. \(2021\)](#).

Chapter 4

EVN follow-up study of milli-lens candidates

The sources included in the 40 best candidates in the Astrogateo database were subsequently proposed for further EVN observations at 5 GHz and 22 GHz. Here our analysis is mainly based on the 5 GHz data of a number of these sources. These follow-up observations are meant to discern some cases where, because of the limited sensitivity of the images used in the pilot program, it was not possible to tell apart core-jet structures from multiple compact component sources. Additionally, thanks to the higher resolution of observations at 22 GHz we are able to determine the structure of the components in even more detail. From the 16 sources we studied in this thesis, the following were included in the 40 best lens candidates from the Astrogateo data:

| J2000 Name | J2000 Coordinates |
|------------|----------------------------|
| J0213+8717 | 02:13:57.846 +87:17:28.726 |
| J0237+1116 | 02:37:13.590 +11:16:15.477 |
| J0527+1743 | 05:27:23.235 +17:43:25.044 |
| J0616-1957 | 06:16:01.601 -19:57:16.223 |
| J0732+6023 | 07:32:50.970 +60:23:40.060 |
| J1132+5100 | 11:32:50.385 +51:00:19.919 |
| J1143+1834 | 11:43:26.070 +18:34:38.360 |
| J1306+0341 | 13:06:15.969 +03:41:38.232 |
| J1344-1739 | 13:44:03.424 -17:39:05.672 |

TABLE 4.1: Sources included in the 40 best lens candidates from the Astrogateo database

All these sources, in addition to being formed by two or more distinct compact structures with milli-arcseconds separations, have also passed some initial tests, like the SB preservation criterion. The rest of the sources in this work have a multiple components structure as well, but were already discarded since they did not pass the SB preservation criterion. The reason we include the latter sources is mainly to confirm these results using our new, more precise EVN data.

4.1 Very Long Baseline Interferometry data

The VLBI data used in this work resulted from the coordinated operation of a network of multiple telescopes around the globe. The EVN consists of more than 20 telescopes, located in Europe, Asia and one antenna in South Africa. Each pair of antennas forms an interferometer whose angular resolution is given by the distance between the two antennas, that is called a *baseline*.

The angular resolution, θ , in the case of a single antenna, depends on the wavelength of the observed signal and the diameter D of the dish according to the relation:

$$\theta \sim \frac{\lambda}{D} \quad (4.1)$$

In the case of a two antenna interferometer this dependence has the same form with the only difference that the quantity D corresponds to the length of the baseline. While long baselines give us an idea of the resolution power of an interferometer, short baselines are more sensitive to extended emission and tell us what is the most extended structure detectable. Hence, interferometers with short baselines can give us an idea of a source's general structure. Longer baselines, instead, provide information on the finer details of the source.

This type of interferometry is called *aperture synthesis* and enables us to use a number of smaller antennas located in great distances away from each other in order to get images with much greater resolution than that of the biggest antennas that we are able to build. More specifically, we get an angular resolution corresponding to the longest baseline available in our network that, in the case of VLBI, can be close to the diameter of the Earth. Preferably, a system of antennas should cover a variety of different baselines in order to have the most complete image possible of the source's structure and finer details.

During each observing session every antenna records the electromagnetic field coming from the observed source. This happens without a direct contact between the different antennas and with the use of precise atomic clocks. Subsequently the data are transferred to the correlator center, where the signals from the different stations get cross-correlated. At this stage, the bulk of *delays*, i.e. variations of phase over frequency, and *rates*, i.e. variations of phase over time, are corrected. Delays mostly come from the different arrival times of the electromagnetic waves at the various observing stations because of their different positions on the Earth's surface with respect to the direction of the incoming signal of the source. We refer to the correlator output with the term (*fringe*) *visibility function*, $V(u,v)$, where u and v are the coordinates of what we call *uv-plane*. This plane helps us displaying the Fourier transforms of the received signal and is defined as being tangent to the celestial sphere at the position of the observed astronomical object. The u -axis denotes the west-east direction, while the v -axis denotes the south-north direction on the plane. The two axes are scaled so that the wavelength of the observed wave is the unit of distance. Each measurement/data point corresponds to a pair of antennas and their relative position is portrayed in the uv plot in the way an observer located in the source would see them. We get both the value of $V(u,v)$ and its complex conjugate $V^*(-u,-v)$ that correspond to two symmetric points with respect to the center of the uv plot. These points are equivalent because, according to the Fourier transform theory, they correspond to the same spacial frequency measurement. Images from VLBI data are unique in the sense that they are not captured in pixel space like with a regular camera, but rather in frequency space. What we observe is the source's brightness distribution over a finite radio bandwidth, convolved with the Point Spread Function (PSF) or beam of the observing instrument (its response to the observation of a point source at the center of the field.)

Of course the reliance just on the number of antennas and the pairs they can form is bound to lead to a incomplete uv coverage, with a great number of intermediate frequencies missing. This is because it is impossible to cover the whole globe with antennas. What generally makes the VLBI technique particularly useful is that we can use the Earth's rotation to fill more points in the uv -plane, since it changes the relative position of the antennas as seen by the source. In this way, with consecutive observations of the same source and despite using the same antenna arrangement we are able to improve and expand our data set. An example of a uv plot that was used in this work can be seen in Figure 4.1.

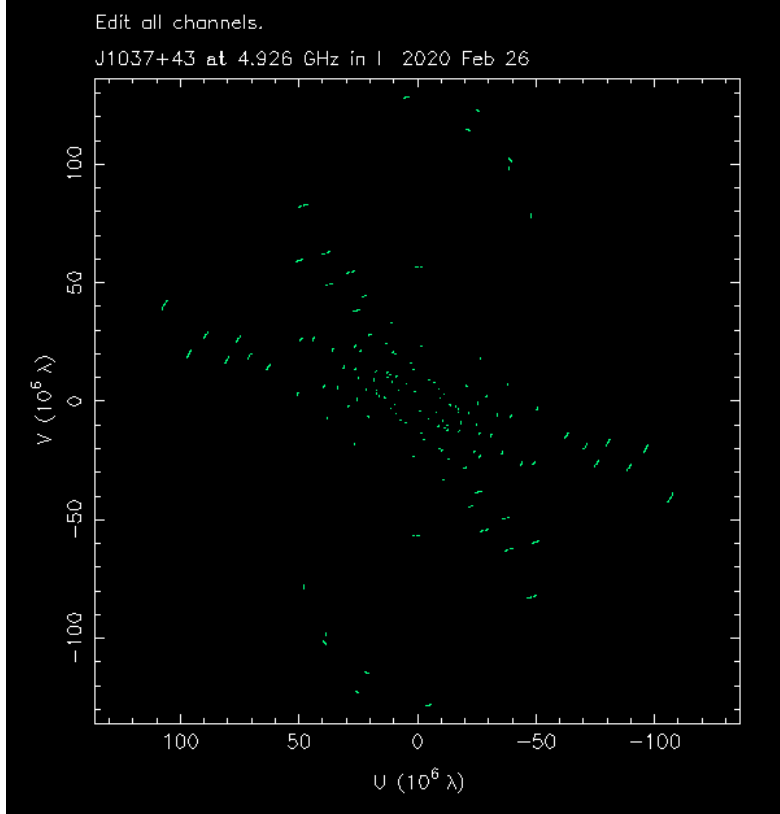


FIGURE 4.1: The uv plot of J1037+4335 during the epoch 26/02/2020 observed at 4.926 GHz

Of course for an optimal data set we would require the whole uv plot to be completely covered with data points (measurements at all available spacial frequencies), as this would lead to a total and unique reconstruction of the source's brightness distribution after a simple inverse Fourier transformation of the measured complex visibilities. Realistically this is not possible to achieve due to the limited number of antennas, hence the uv-coverage is sparsely sampled and the resulting image after the correlation is always expected to be imperfect/dirty. For this reason there is no unique solution for the image reconstruction, making it of major importance that we find a way to reconstruct the image as carefully and accurately as possible by adequately interpolating the visibility data.

4.2 Phase and amplitude calibration

The aforementioned correlation process, despite achieving essential corrections to our data, is not sufficient to reach the imaging step, and usually the phases and amplitudes of the visibility functions need further calibration steps. Lack of proper calibration can lead to the presence

of artifacts in our image that do not correspond to a real structure. The phase and amplitude calibration process was achieved using the Astronomical Image Processing System.

Errors related to the phase usually stem from atmosphere-related effects. We make use of the Global Position System models in order to correct the dispersive delays in the ionosphere and the Earth Orientation Parameters to account for things like the orientation of the antennas while the Earth rotates. We also note that, when dealing with sources of sufficient brightness we can use a process called *fringe-fitting* to determine the phase corrections. Usually, it can be applied on the observed source itself (Schwab & Cotton 1983). However, in our case, the target sources are not bright enough and the phase solutions are determined using nearby bright sources as calibrators. This process is called *phase-referencing*.

For the amplitudes' calibration we make use of the Gain Curve and the System Temperature calibration tables provided by each antenna, that account for the antenna efficiency and the antenna temperature, respectively. Both of these measurements are required in order to convert from the measured antenna temperature (in Kelvin) to the source's flux density (in Jansky). The unit Jansky (Jy) corresponds to $1\text{Jy} = 10^{-26}\text{Wm}^{-2}\text{Hz}^{-1}$.

4.3 Imaging and self-calibration

After the phase and amplitude calibration is completed we are left with the *dirty image*, that is the real image of the source in the sky, convolved with our synthesized beam. In order to move from the dirty image to the real image of the observed source we proceed with the *imaging and self-calibration* stage. This process is achieved mainly using Differential Mapping (Difmap) software. In this case the algorithm that was selected is the CLEAN algorithm presented in Högbom (1974), which is the most commonly used method for image reconstruction.

According to this method, we are able to converge to a final clean image through an iterative process. At each step the user can select boxes (*clean boxes*) where the CLEAN algorithm will search for the intensity peak, convolve it with the dirty beam, and finally subtract it from the dirty image. At the same time, the intensities of the subtracted point-like components, as well as their positions in the image, are saved in a model. This process gets repeated until the flux intensity of the peak has a value close to that of the noise of the image. Practically this means that the process is terminated when it is not possible to tell the intensity peaks apart from the background noise of the image with a visual inspection. Afterwards, the point-like components

in the clean model are convolved with a *clean beam*, that usually corresponds to a Gaussian function fitted to the central lobe of the dirty beam. The value of the FWHM of this Gaussian is equal to that of the dirty beam, allowing for the preservation of the proper angular resolution of the image. After the convolution, the components are added to the last residual map, generating the final image of the source.

The Figures 4.2 and 4.3 are indicative examples of a final residual map and a clean/final image, respectively. Both of them were derived during the imaging and self-calibration process for J0527+1743 at 4.926 GHz, using data from the observing epoch 28 October, 2019. The final residual map (Figure 4.2) is quite uniform, indicating that the iterative process of imaging can be terminated. The final model for this source (Figure 4.3) is presented with the cleaning boxes displayed on top of the image.

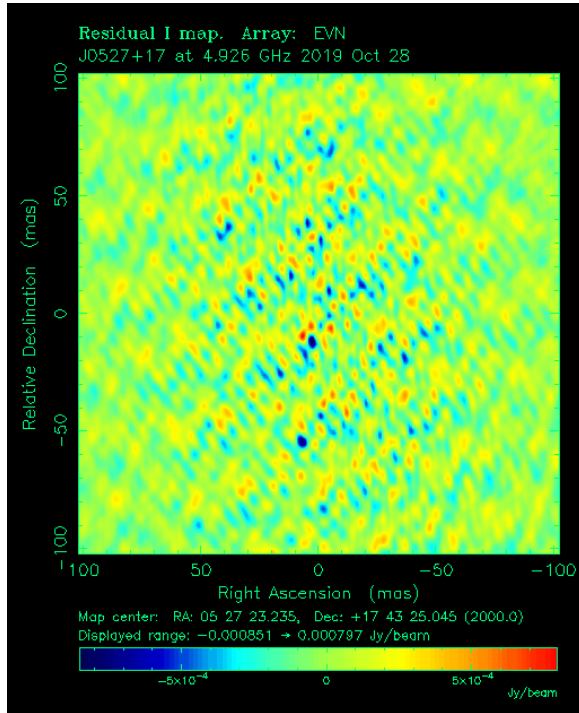


FIGURE 4.2: The final residual map of J0527+1743

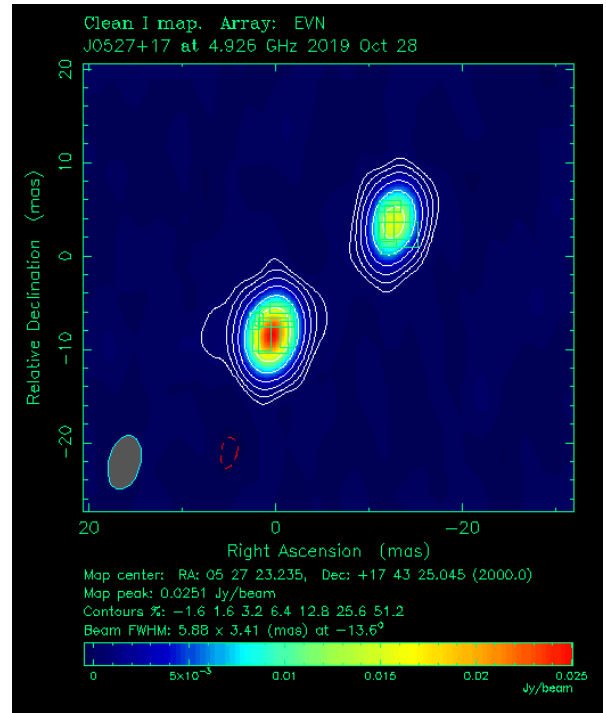


FIGURE 4.3: The clean map of J0527+1743

Finally, it is worth noting that the noise root mean square (rms) that was used in the analysis of some of the sources in this work was measured using Difmap. We use multiple windows that we place in various locations away from the source to take the value of the rms in different parts of the background. The final value of the background noise is the average value of the different rms measurements.

4.4 Model Fitting

After we have reached an ideal clean map of our source, we proceed with a quantitative analysis of its characteristics. Through the *model-fitting* process we can represent its brightness distribution using a number of Gaussian components and extract information on their flux density, FWHM, and position.

The program we are using here makes use of least squares algorithms, meaning we aim at minimising the χ^2 (chi-square) function. The user can set the approximate radius and position of either circular or elliptical components that are used to represent the source structure. The brightness distribution within each component is subsequently fitted using a Gaussian function. The user can then run a `modelfit` command with a set number of iterations. The process terminates when the brightest component in the residual map reaches the same flux density level as the noise. The optimum modelfit has a reduced chi-square value close to 1 and the least number of model components possible. After the completion of this process the algorithm provides us, among others, the flux density, polar coordinates, and (major) FWHM of every individual component. All of these measurements are required in order to calculate important quantities, like the SB of the components or the distances between them.

4.5 Data Analysis

The sources we study here were selected based on their morphology, made of two or more compact structures at milli-arcsecond scales, as they should resemble a milli-lens system. For a number of sources some of these structures had to be modelled using multiple circular Gaussian components in order to achieve the optimum model. We can obtain an estimate of the total flux density of these features by summing up the flux densities of their individual components.

$$F_{tot} = F_1 + F_2 + \dots + F_n \quad (4.2)$$

In the same way, we measure the total area covered by each feature by taking the sum of the areas of these single components. For circular Gaussian components the FWHM value corresponds to, approximately, the diameter of the model component, so we can derive the area of a component by taking its square value. We can use this to derive the following relation for the area of a structure:

$$Area_{tot} = (FWHM_1)^2 + (FWHM_2)^2 + \dots + (FWHM_n)^2 \quad (4.3)$$

where $FWHM_1, FWHM_2, \dots, FWHM_n$ are the values of the FWHM of each component in the case a structure is represented by n number of model components.

In order for us to be able to classify a source as a good lens system candidate its physical quantities should adhere to specific criteria. More specifically we demand that our candidates obey the *flux density ratio preservation* among epochs, the *surface brightness preservation criterion*, the *spectral indexes criterion*, as well as pass some additional visual inspection tests and preserve the distance between components among epochs. We will examine each individual criterion in more detail below.

Flux Density Ratio Preservation Criterion

In cases of gravitational lens systems the flux ratio (FR) between the two main structures at a single frequency is preserved among epochs, as long as time delays between images are irrelevant like in the case of lenses at milliarcsecond scales. We define the FR as the ratio of the flux density of the brightest component (component A) over the faintest one (component B), therefore it should always have a value greater than 1.

$$FR = \frac{F_A}{F_B} \quad (4.4)$$

For the purposes of our analysis we set as an upper bound for what we consider an acceptable deviation between two FR values computed at two different epochs, equal to the combined error:

$$\delta FR = \sqrt{(\delta FR_1)^2 + (\delta FR_2)^2} \quad (4.5)$$

where δFR_1 and δFR_2 are the FR errors at the two epochs. These errors are calculated by propagating the uncertainties of the flux density values, which are in turn obtained as follows (Oriente & Dallacasa 2020):

$$\delta F = \sqrt{\delta F_{cal}^2 + \delta F_{rms}^2} \quad (4.6)$$

Here, the term δF_{cal} is typically equal to 10% the flux density value of the component and is an added error stemming from the amplitude calibration (Casadio et al. 2019). The term δF_{rms} instead refers to the rms that is measured on the background of each source. For the latest

images that were produced in this work the rms was measured as described in Section 4.3. For the previous epochs we used the available Astrogio data to determine the mean rms value in each frequency band.

Surface Brightness Preservation Criterion

Another important factor to consider in our search for lens system candidates is the SB preservation criterion between the two compact structures. If we assume that both compact structures are images of the same bright source, we expect the one with the smaller flux density value to also be more compact.

The SB of a component is defined by the relation:

$$SB = \frac{Total\ Flux}{Total\ Area} \quad (4.7)$$

For a lens system the SB ratio between the two images should have a value close to 1. Here we define the SB ratio in a way so that it takes values greater than 1. We also set an upper bound of what we accept as an SB ratio value to be equal to 4 in accordance to what was used in Browne et al. (2003). The same upper limit in the pilot project was equal to 7, but here our newest data has better precision and a more conservative value is better if we want to narrow our sources down to the best lens candidates. Any source with SB ratio greater than this can be immediately discarded. Generally the brightest component (component A) is also the one with larger SB value, except for the case of the source J1132+5100.

The SB ratio error δSB_{ratio} is calculated using error propagation theory and the formula for SB expressed above. As an error for the FWHM of each component we set the minimum resolvable size as calculated for the image in each observational epoch. This is derived from the equation used in Nair et al. (2019) and Lobanov (2005):

$$d_{min} = \frac{2}{\pi} \left[\pi \alpha \beta \log \left(\frac{\frac{S}{N} + 1}{\frac{S}{N}} \right) \right]^{\frac{1}{2}} \quad (4.8)$$

for images with normal weighting, which is the case for every image in this work. Here α and β are defined as the minor and major axes of the restoring beam, while $\frac{S}{N}$ is the signal to noise ratio

of our image, which is defined as the flux of the brightest component of the image (component A), over the rms of the background.

Spectral Indexes Criterion

One more feature we want to check is the *spectral indexes criterion*. The spectral index, α , is the index of the power law describing the relation between the flux density and the frequency, and is defined through the relation 2.2. In order to calculate the spectral index between the two frequencies ν_1 and ν_2 we use the following equation:

$$\alpha = \frac{\log_{10}(F_1/F_2)}{\log_{10}(\nu_1/\nu_2)} \quad (4.9)$$

where F_1 and F_2 are the flux densities of the component as measured at the two respective frequencies, and at the same epoch. According to the spectral indexes criterion, we expect the two components to have similar spectral indexes, if we are dealing with a gravitational lens system. This is because they are images of the same source and, therefore, the form of their radiation spectrum should be similar. Generally, sources with a component that has a much steeper spectrum than the other most likely point towards the core and jet structure of an AGN and, thus, can be discarded as lens candidates.

Visual Inspection and Distance Between Components

A visual inspection of the source, once the image is obtained, is always the first test to discriminate between core+jet structures or possible artifacts. Additionally, we are careful when dealing with structures that are not preserved between epochs, since they could correspond to artifacts.

In two of the sources that seem to satisfy all the aforementioned criteria, we also calculated the distance between their two brightest components in the EVN images at 5 GHz, and we compared it with the same distance measured for a previous observational epoch. The model-fitting process provides us the positions of the different components expressed in polar coordinates, meaning

that the distance we are trying to calculate can be derived using the relation:

$$L = \sqrt{r_1^2 + r_2^2 - 2 r_1 r_2 \cos(\theta_1 - \theta_2)} \quad (4.10)$$

where we denote the coordinates of one of the points as (r_1, θ_1) and the other (r_2, θ_2) . Here the radii r_1 and r_2 are expressed in milliarcseconds, while the angles θ_1 and θ_2 in radians. Our goal is to check whether the two components are stationary over time, or they display some motion. In a gravitational lens system we would expect them to have the same distance over epochs, since it depends on factors like the distance of the source from the lens, or characteristics of the lens itself, like its mass and geometry, that we don't expect to change rapidly. For cases of detected motion of the components this would probably point towards a core+jet scenario. For the uncertainty on the distance we use the minimum resolvable size d_{min} as presented above.

Chapter 5

Results

In this section each of the sources that were studied are presented individually, with their new images obtained with the EVN array. They were constructed from the visibilities after a self calibration stage and with the use of clean components, as described in Chapter 4.3. Images from the Astrogéo data are also presented here as a comparison for our new observations. They display multiple frequencies overlaid on top of each other on the same plot and they have circular restoring beams with diameter that is dictated by the minor and major axis of the original restoring beams of the image FITS files. More specifically:

$$d_{new} = \sqrt{d_{minor} * d_{major}} \quad (5.1)$$

Therefore, for sources for which multi-epoch observations took place, the image is a result of the convolution of the visibilities with a median circular beam and the averaging of these images for all available epochs. Sources with just one available epoch are presented with the original elliptical beam.

On top of the new EVN 5 GHz images we display the model-fit components, which generally appear as red circles with diameter equal to the corresponding FWHM, except for FWHM values smaller than the minimum resolvable size, which are instead displayed as red crosses.

In the case of sources in which the model fit has just two model components, these components are simply denoted as component "A" and component "B" in the new images, with component A being the brightest of the two, in accordance with the notation in the Astrogéo data images used in the pilot search. When one or both compact structures are model-fitted with more than

a single model component we label each individual component separately. We denote as A0 (or B0 respectively) the brightest component, that usually corresponds to the one closest to the core of the structure, and A1, A2, A3, ..., An (or B1, B2, B3, ..., Bn) the rest of them, where n is the total number of additional model components. In every case, the physical properties of the structures are collected in tables, where we denote as components A and B the two main compact structures as a whole, independently of the number of the model components considered. For multiple-component structures the total flux density and area are calculated using equations 4.2 and 4.3. A source is judged as a good lens candidate only if it passes successfully all the tests proposed in Section 4.5.

5.1 J0213+8717

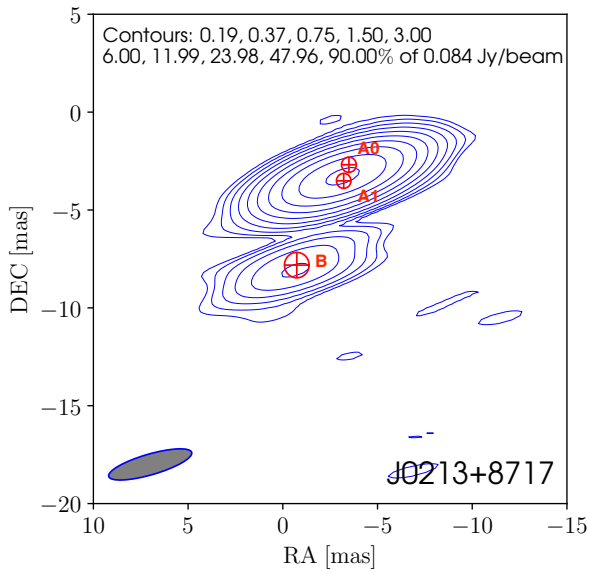


FIGURE 5.1: J0213+8717 EVN 5 GHz data

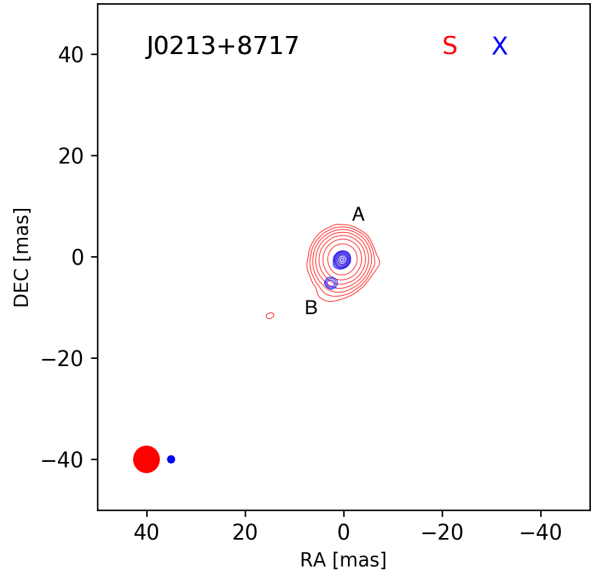


FIGURE 5.2: J0213+8717 Astrogéo data at 2.3 GHz (S-band) and 8 GHz (X-band)

| Epochs | Frequency (GHz) | Component | Flux (Jy) | Flux Ratio | Error | FWHM (milli-arcsec) | Error (milli-arcsec) | SB (Jy/arcsec ²) | SB Ratio | Error |
|------------|--------------------|-----------|--------------|---------------|-------|------------------------|-------------------------|---------------------------------|-------------|-------|
| 2004-04-30 | 8 | A | 1.152E-01 | 7 | 1 | 0.39 | 0.05 | 769E+03 | 1.5 | 0.9 |
| | | B | 1.564E-02 | | | 0.17 | 0.05 | 522E+03 | | |
| 2014-05-31 | 8 | A | 9.003E-02 | 12 | 2 | 0.42 | 0.05 | 502E+03 | 0.3 | 0.4 |
| | | B | 7.716E-03 | | | 0.07 | 0.05 | 1816E+03 | | |
| 2017-03-23 | 8 | A | 0.082E-02 | 13 | 2 | 0.58 | 0.05 | 243E+03 | 3.0 | 1.4 |
| | | B | 6.23E-03 | | | 0.28 | 0.05 | 80E+03 | | |
| 2019-10-28 | 4.926 | A | 1.329E-01 | 14 | 2 | 1.09 | 0.03 | 111E+03 | 19.8 | 3.1 |
| | | B | 9.462E-03 | | | 1.30 | 0.03 | 6E+03 | | |

TABLE 5.1: J0213+8717

Here we should note that just for the second epoch the value of the SB ratio for this source is below 1, which means that in this observation component B has a larger SB than component A.

Despite the limited resolution of the Astrogéo data in the S-band that doesn't make it easy to tell the two components apart, the observations in the X-band clearly show two distinct components. With the new EVN 5 GHz data we are able to reveal more details of the source's image and we can notice that the two components of the structure do not appear to be entirely separated, as we initially assumed.

The value of the FR at 8 GHz increases with each consecutive epoch significantly leading to a big deviation between the first measured value and the latest ones. Notably, the values of the first and the third epoch are not in agreement within errors. Moreover, although the SB ratio values in the first three epochs are within the considered upper limit, for the last epoch SB is greater than 4. We can conclude that both the FR and SB are not passing the tests, hence the source is not a good lens candidate.

5.2 J0237+1116

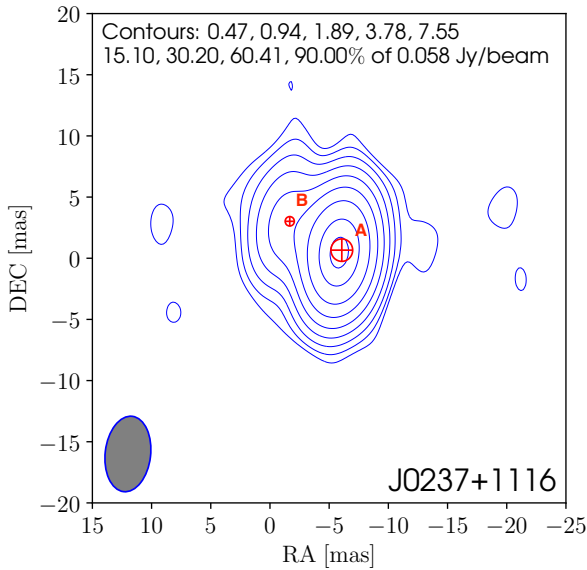


FIGURE 5.3: J0237+1116 EVN 5 GHz data

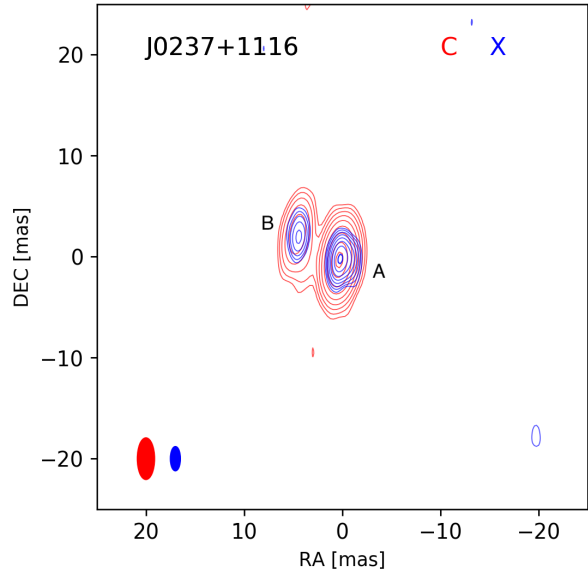


FIGURE 5.4: J0237+1116 Astrogéo data at 4.3 GHz (C-band) and 8 GHz (X-band)

For this source we can notice that, although initially the image seems to suggest two distinct components in both the C and X-band, in the new EVN data we can see a quite uniform structure.

| Epochs | Frequency (GHz) | Component | Flux (Jy) | Flux Ratio | Error | FWHM (milli-arcsec) | Error (milli-arcsec) | SB (Jy/arcsec ²) | SB Ratio | Error |
|------------|--------------------|-----------|--------------|---------------|-------|------------------------|-------------------------|---------------------------------|-------------|-------|
| 2016-05-27 | 4.3 | A | 7.55E-02 | 8 | 1 | 0.70 | 0.07 | 152E+03 | 3.0 | 1.2 |
| | | B | 9.96E-03 | | | 0.45 | 0.07 | 50E+03 | | |
| 2016-05-27 | 8 | A | 6.25E-02 | 8 | 1 | 0.94 | 0.04 | 70E+03 | 4.3 | 0.9 |
| | | B | 7.87E-03 | | | 0.70 | 0.04 | 16E+03 | | |
| 2019-10-28 | 4.926 | A | 6.04E-02 | 9 | 1 | 1.84 | 0.12 | 18E+03 | 1.6 | 0.6 |
| | | B | 6.754E-03 | | | 0.77 | 0.12 | 11E+03 | | |

TABLE 5.2: J0237+1116

The form of the source according to the latest epoch could point to a core+jet structure instead of a gravitational system.

The FR values in the two observations at 4.3 and 5 GHz (C-band) are in agreement within errors, which means that the FR between the two components is preserved in time.

As an additional test for this source we calculated the distance between the two brightest components for both the older and the newer epoch at 5 GHz and found them 4.97 ± 0.07 mas and 5.0 ± 0.1 mas, respectively. The two distances agree within errors, hence the two components do not show relative motion between these two observational epochs. This source could still be a gravitational lens candidate, and more in depth analysis needs to be carried out.

5.3 J0455-2034

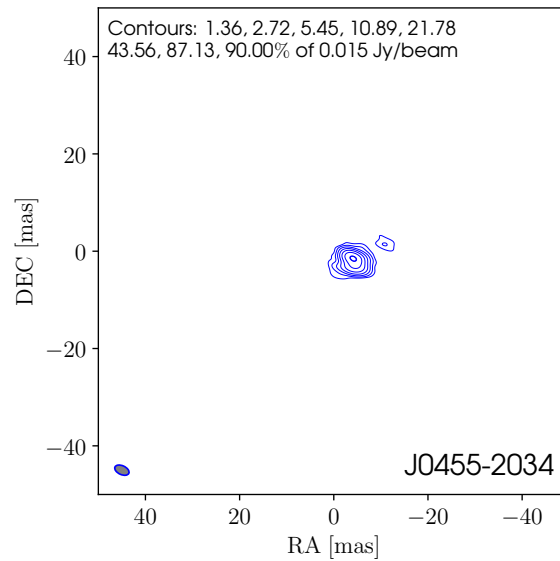


FIGURE 5.5: J0455-2034 EVN 5 GHz data

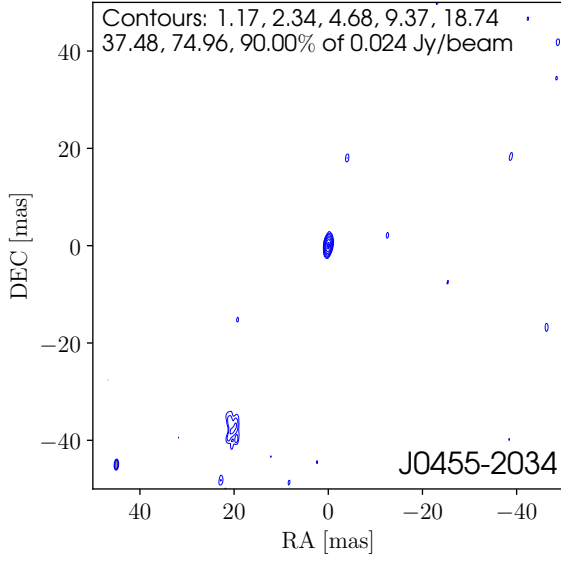


FIGURE 5.6: J0455-2034 2010/12/21
Astrogeo data at 8 GHz (X-band)

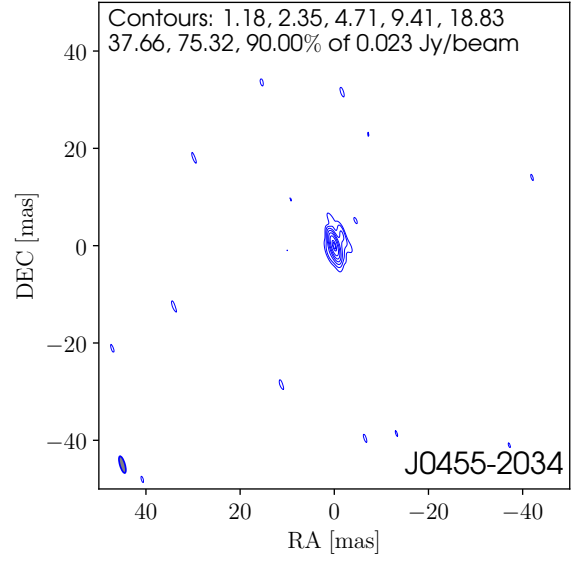


FIGURE 5.7: J0455-2034 2011/01/13
Astrogeo data at 8 GHz (X-band)

This source was not initially included in the 40 best candidates from the Astrogeo database since it does not pass the SB test according to the 8 GHz observation from 2010. The images from the two available epochs (2010/12/21 and 2011/01/13) are shown above and are made so that they have the same field of view. What we can notice when comparing these two is that the second component (component B), although present in the 2010 observations (Figure 5.6), seems to be missing from the 2011 image (Figure 5.7), as well as in the image from the new 5 GHz EVN data (Figure 5.5). It is possible that the secondary component is not a real structure but an artifact. This source continues to be discarded as a lens candidate.

5.4 J0527+1743

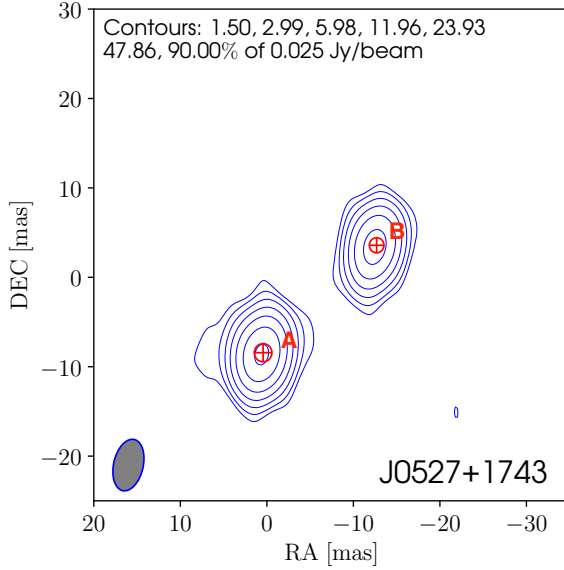


FIGURE 5.8: J0527+1743 EVN 5 GHz data

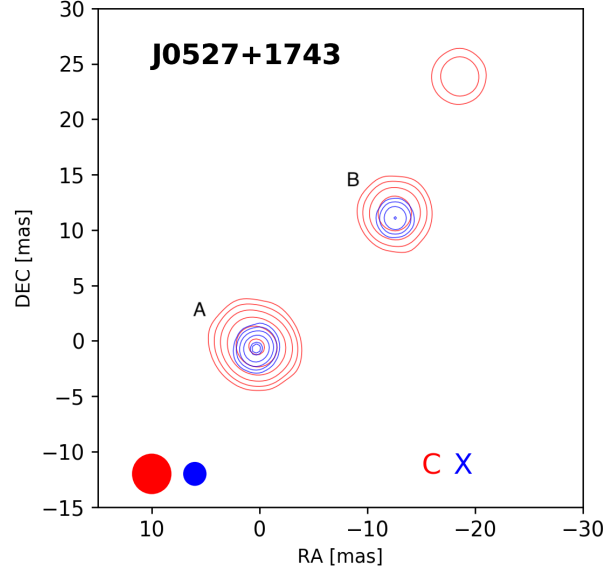


FIGURE 5.9: J0527+1743 Astrogéo data at 4.3 GHz (C-band) and 8 GHz (X-band)

In the case of this source, the third component in the image created using the Astrogéo data is not visible in the new EVN image. This could mean that it is a non-real structure. The subsequent analysis is focused on the two main components A and B as marked in the images.

| Epochs | Frequency (GHz) | Component | Flux (Jy) | Flux Ratio | Error | FWHM (milli-arcsec) | Error (milli-arcsec) | SB (Jy/arcsec ²) | SB Ratio | Error |
|------------|--------------------|-----------|--------------|---------------|-------|------------------------|-------------------------|---------------------------------|-------------|-------|
| 2015-10-30 | 4.3 | A | 2.180E-02 | 2.4 | 0.3 | 1.06 | 0.15 | 19E+03 | 0.72 | 0.42 |
| | | B | 9.271E-03 | | | 0.58 | 0.15 | 27E+03 | | |
| 2015-10-30 | 8 | A | 1.764E-02 | 2.3 | 0.3 | 0.69 | 0.09 | 38E+03 | <0.04 | |
| | | B | 7.726E-03 | | | < 0.09 | 0.09 | >888E+03 | | |
| 2019-10-28 | 4.926 | A | 3.020E-02 | 1.6 | 0.2 | 2.04 | 0.18 | 7E+03 | 1.11 | 0.35 |
| | | B | 1.880E-02 | | | 1.69 | 0.18 | 7E+03 | | |

TABLE 5.3: J0527+1743

The FR values at 5 GHz in the two available epochs diverge significantly. We can conclude that the FR between the two components does not have a constant value among epochs. The SB ratio values in these C-band observations are very close to 1 as we would expect in the case of a gravitational lens system. During the first 5 GHz epoch the SB value of component B is greater than that of the component A, resulting in an SB below 1. It should be noted here that component B in the 2015 observation at 8 GHz, has a FWHM that is below the minimum resolvable size. As a result, the SB ratio for this observation refers to an upper bound, instead of an exact value. Even then, the SB ratio value for this observation diverges significantly from

the value 1. The aforementioned results lead us to conclude that this source is most likely not a lens candidate.

In any case we also calculated the distance between the two components in the two images at 5 GHz and we found them equal to 17.6 ± 0.1 mas and 17.8 ± 0.2 mas, respectively. The deviation between the two values is smaller than the combined error and, therefore, the two components can be considered stationary within the 4 years spanned by the two epochs.

5.5 J0602-2546

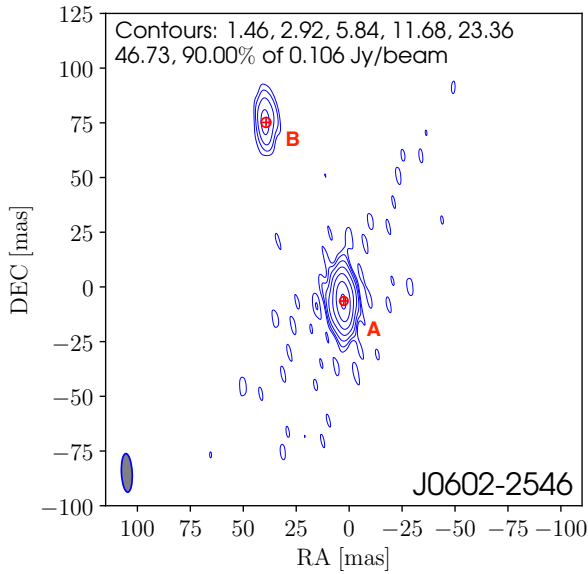


FIGURE 5.10: J0602-2546 EVN 5 GHz data

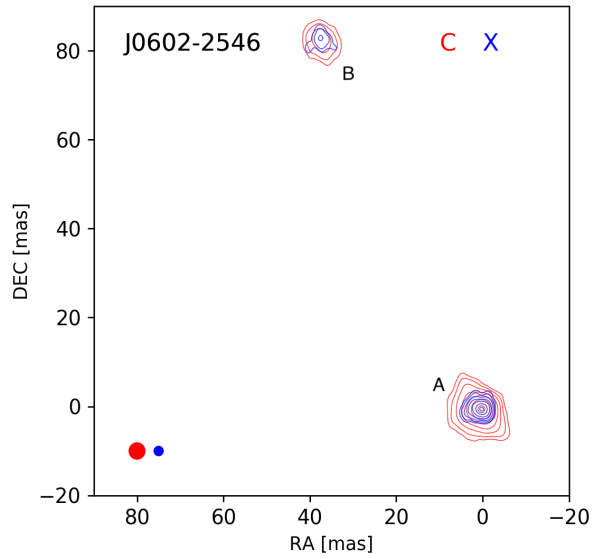


FIGURE 5.11: J0602-2546 Astrogro data at 4.3 GHz (C-band) and 8 GHz (X-band)

| Epochs | Frequency (GHz) | Component | Flux (Jy) | Flux Ratio | Error | FWHM (milli-arcsec) | Error (milli-arcsec) | SB (Jy/arcsec ²) | SB Ratio | Error |
|------------|--------------------|-----------|--------------|---------------|-------|------------------------|-------------------------|---------------------------------|-------------|-------|
| 2015-08-27 | 4.3 | A | 1.349E-01 | 6.5 | 0.9 | 2.96 | 0.09 | 15E+03 | 8 | 1 |
| | | B | 2.069E-02 | | | 3.36 | 0.09 | 2E+03 | | |
| 2015-08-27 | 8 | A | 8.287E-02 | 9.1 | 1.3 | 2.50 | 0.05 | 13E+03 | 13 | 2 |
| | | B | 9.148E-03 | | | 2.99 | 0.05 | 1E+03 | | |
| 2016-07-17 | 4.3 | A | 1.325E-01 | 6.6 | 0.9 | 2.58 | 0.09 | 20E+03 | 14 | 2 |
| | | B | 2.006E-02 | | | 3.75 | 0.09 | 1E+03 | | |
| 2016-07-17 | 8 | A | 8.568E-02 | 7.9 | 1.1 | 2.49 | 0.05 | 14E+03 | 12 | 2 |
| | | B | 1.081E-02 | | | 3.05 | 0.05 | 1E+03 | | |
| 2019-10-28 | 4.926 | A | 1.281E-01 | 5.9 | 0.8 | 3.96 | 0.44 | 8E+03 | 8 | 3 |
| | | B | 2.185E-02 | | | 4.53 | 0.44 | 1E+03 | | |

TABLE 5.4: J0602-2546

The values of the FR in the three observations at 4.3 GHz, as well as the ones at 8 GHz, are in agreement within errors. It is clear that for this source the FR is preserved among different

epochs. However, the SB ratio for all available observational epochs has values much greater than 4, making it obvious that this source does not obey the SB conservation criterion and, therefore, is not a good lens candidate. This result confirms our original choice of not listing this particular source among the 40 most probable lens candidates.

5.6 J0616-1957

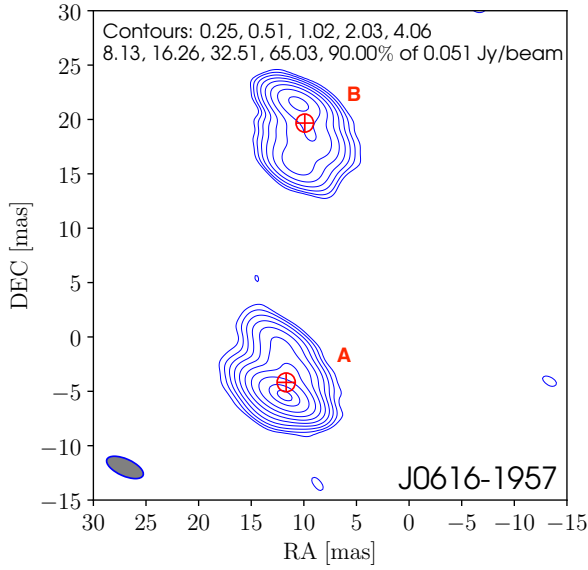


FIGURE 5.12: J0616-1957 EVN 5 GHz data

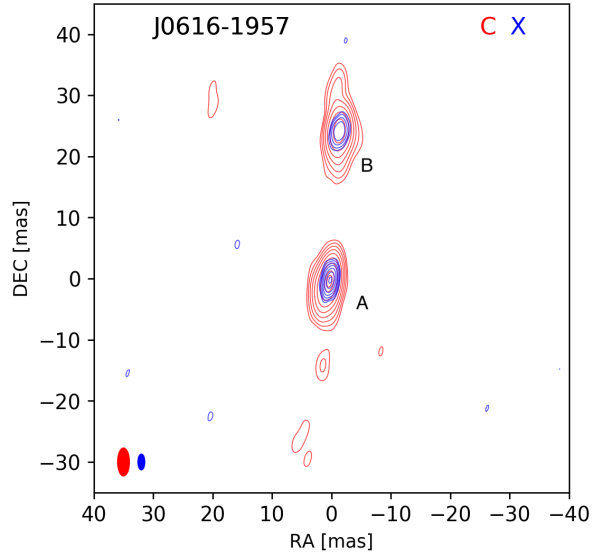


FIGURE 5.13: J0616-1957 Astrogéo data at 4.3 GHz (C-band) and 8 GHz (X-band)

| Epochs | Frequency (GHz) | Component | Flux (Jy) | Flux Ratio | Error | FWHM (milli-arcsec) | Error (milli-arcsec) | SB (Jy/arcsec ²) | SB Ratio | Error |
|------------|-----------------|-----------|-----------|------------|-------|---------------------|----------------------|------------------------------|----------|-------|
| 2016-01-20 | 4.3 | A | 8.378E-02 | 1.6 | 0.2 | 1.44 | 0.07 | 41E+03 | 2.3 | 0.4 |
| | | B | 5.122E-02 | | | 1.69 | 0.07 | 18E+03 | | |
| 2016-01-20 | 8 | A | 3.304E-02 | 2.5 | 0.4 | 0.89 | 0.07 | 41E+03 | 8.5 | 1.9 |
| | | B | 1.321E-02 | | | 1.65 | 0.07 | 5E+03 | | |
| 2019-10-28 | 4.926 | A | 8.648E-02 | 1.8 | 0.3 | 1.73 | 0.03 | 3E+03 | 1.6 | 0.3 |
| | | B | 4.876E-02 | | | 1.66 | 0.03 | 2E+03 | | |

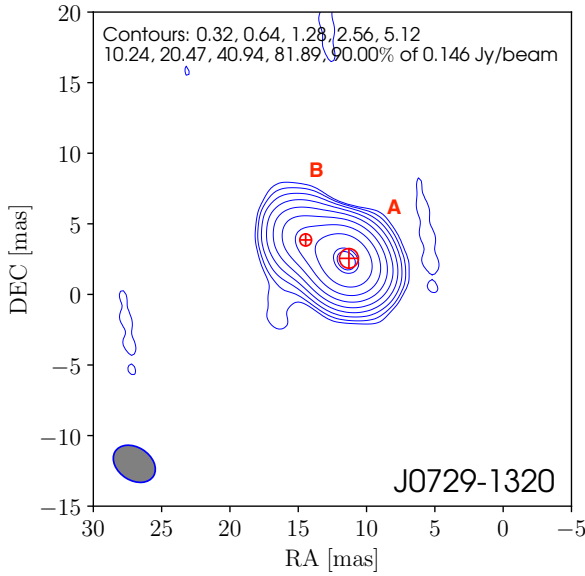
TABLE 5.5: J0616-1957

Our new 5 GHz data has higher resolution in the north-south direction. The image reveals extended jet-like structures in both components that seem to be pointing towards a common center.

The FR values at the two closest frequencies 4.3 GHz and 4.9 GHz have a deviation equal to 0.4 times the combined error, which is acceptable. Additionally, in all observations at the C-band, the SB ratios have values smaller than 4. Nevertheless, at 8 GHz, the SB ratio is greater than

4 by more than twice the error. The SB is not preserved between the two components in this source. Moreover, the spectral indexes of the two components, computed considering the 4.3 and 8 GHz data in 2016, are -1.5 and -2.2, thus implying very steep spectra. This result goes against a gravitational lens prediction. For the aforementioned reasons we discarded this source.

5.7 J0729-1320



are much greater than 4. For these reasons we can discard this source since it cannot be a gravitational lens candidate.

5.8 J0732+6023

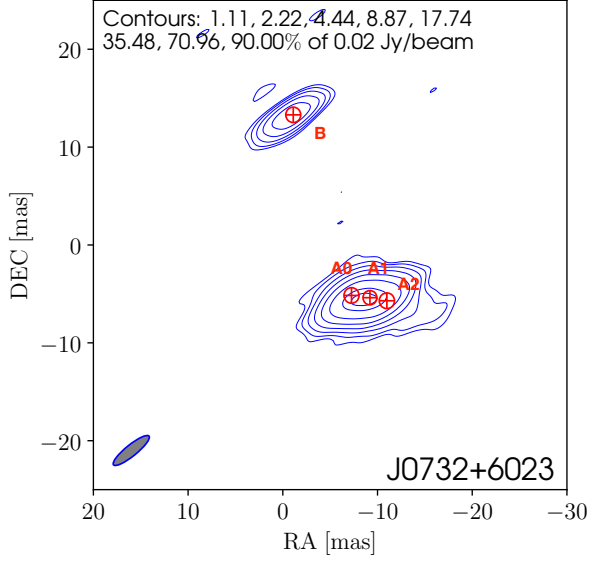


FIGURE 5.16: J0732+6023 EVN 5 GHz data

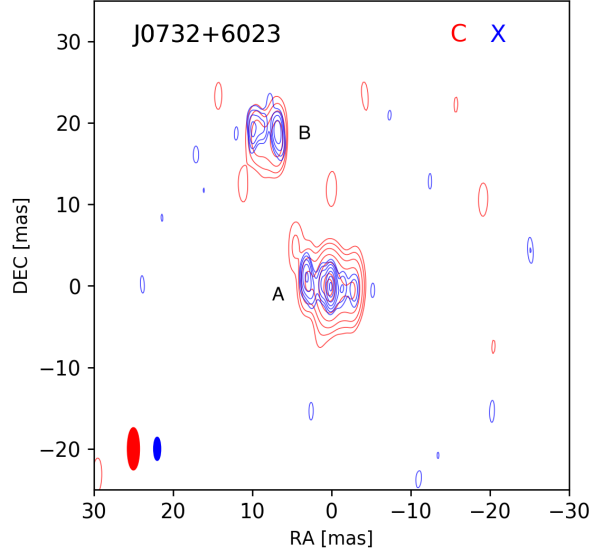


FIGURE 5.17: J0732+6023 Astrogoo data at 4.3 GHz (C-band) and 8 GHz (X-band)

| Epochs | Frequency (GHz) | Component | Flux (Jy) | Flux Ratio | Error | FWHM (milli-arcsec) | Error (milli-arcsec) | SB (Jy/arcsec ²) | SB Ratio | Error |
|------------|--------------------|-----------|--------------|---------------|-------|------------------------|-------------------------|---------------------------------|-------------|-------|
| 2016-08-11 | 4.3 | A | 4.377E-02 | 2.9 | 0.4 | 1.61 | 0.14 | 17E+03 | 1.9 | 0.6 |
| | | B | 1.503E-02 | | | 1.31 | 0.14 | 9E+03 | | |
| 2016-08-11 | 8 | A | 1.628E-02 | 1.2 | 0.2 | 0.39 | 0.07 | 107E+03 | 76.3 | 30.5 |
| | | B | 1.321E-02 | | | 3.07 | 0.07 | 1E+03 | | |
| 2019-10-28 | 4.926 | A | 6.442E-02 | 7.1 | 1.0 | 2.69 | 0.05 | 9E+03 | 2.4 | 0.4 |
| | | B | 9.092E-03 | | | 1.58 | 0.05 | 4E+03 | | |

TABLE 5.7: J0732+6023

The FR deviation value between the first and latest epoch at the C-band is calculated to be greater than three times the combined error, hence the FR at this specific frequency is not preserved among epochs. Moreover, the SB ratio does not fulfill the conditions requested. This is because, in the case of the 8 GHz observation, the SB ratio value is well above 4 even considering uncertainties. This source is not a good lens candidate.

5.9 J0840-0648

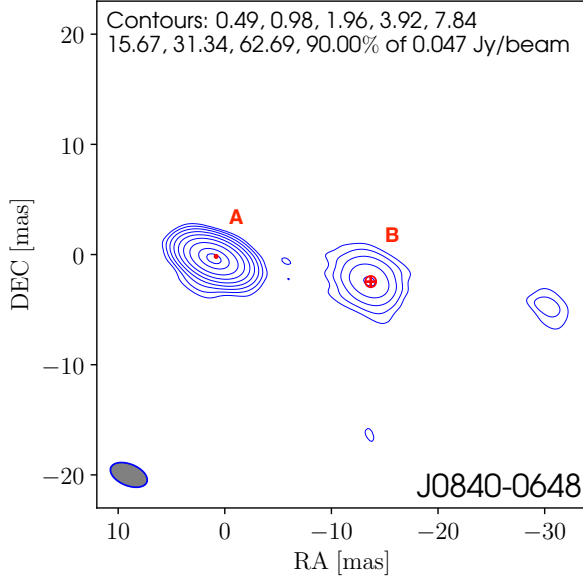


FIGURE 5.18: J0840-0648 EVN 5 GHz data

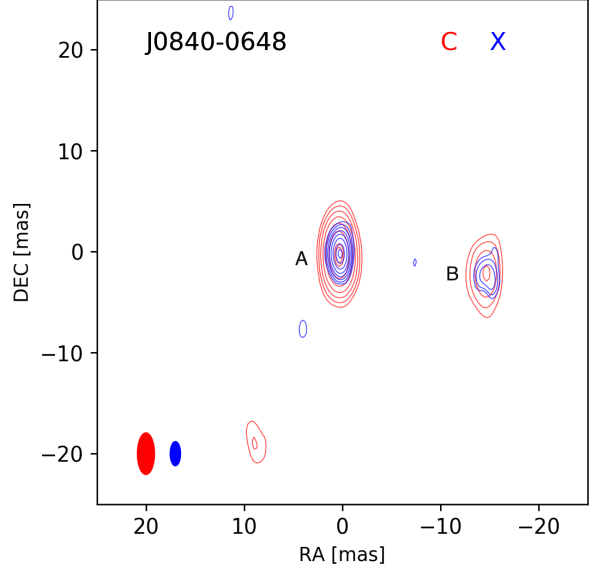


FIGURE 5.19: J0840-0648 Astrogro data at 4.3 GHz (C-band) and 8 GHz (X-band)

| Epochs | Frequency (GHz) | Component | Flux (Jy) | Flux Ratio | Error | FWHM (milli-arcsec) | Error (milli-arcsec) | SB (Jy/arcsec ²) | SB Ratio | Error |
|------------|--------------------|-----------|--------------|---------------|-------|------------------------|-------------------------|---------------------------------|-------------|-------|
| 2015-10-13 | 4.3 | A | 5.137E-02 | 6.5 | 0.9 | 0.62 | 0.12 | 135E+03 | 32 | 15 |
| | | B | 7.935E-03 | | | 1.38 | | 4E+03 | | |
| 2015-10-13 | 8 | A | 3.724E-02 | 8.8 | 1.3 | 0.45 | 0.06 | 188E+03 | 57 | 17 |
| | | B | 4.254E-03 | | | 1.13 | | 3E+03 | | |
| 2020-02-26 | 5 | A | 4.735E-02 | 8.1 | 1.1 | 0.29 | 0.07 | 547E+03 | 98 | 51 |
| | | B | 5.856E-03 | | | 1.03 | | 6E+03 | | |

TABLE 5.8: J0840-0648

The FR does not seem to have a constant value for the two epochs at 4.3 and 5 GHz, with a deviation that is 1.1 times the combined error. Additionally, the SB ratio between the two components, for all three available observations has values much greater than 4. This source can be discarded, as it does not seem to satisfy neither the FR, nor the SB criterion.

5.10 J0900-0652

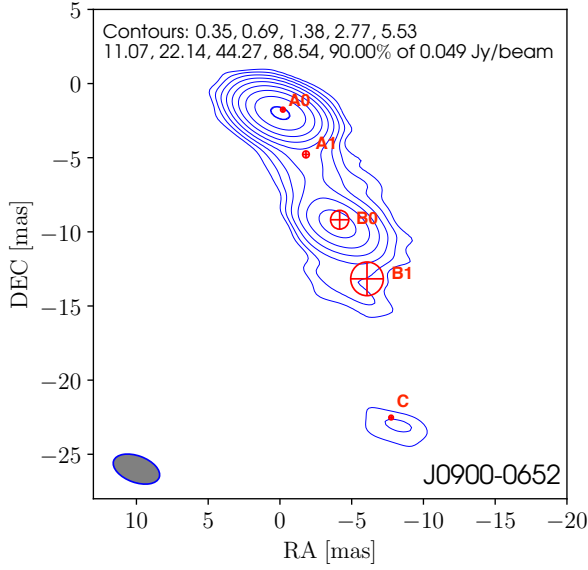


FIGURE 5.20: J0900-0652 EVN 5 GHz data

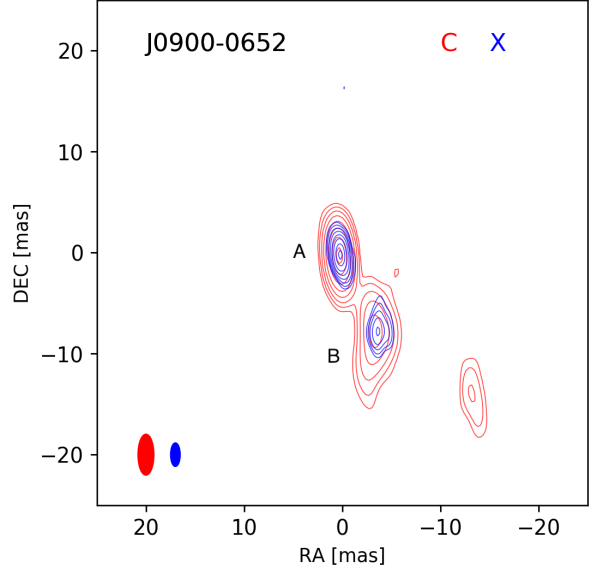


FIGURE 5.21: J0900-0652 Astrogro data at 4.3 GHz (C-band) and 8 GHz (X-band)

Due to the higher sensitivity of the new observation we are able to observe that the two main components are not completely separated, but are connected with an extended structure that could point towards a jet+core structure. Component C is required to have a better model of the source structure, but we do not include it in our analysis.

| Epochs | Frequency (GHz) | Component | Flux (Jy) | Flux Ratio | Error | FWHM (milli-arcsec) | Error (milli-arcsec) | SB (Jy/arcsec ²) | SB Ratio | Error |
|------------|--------------------|-----------|--------------|---------------|-------|------------------------|-------------------------|---------------------------------|-------------|-------|
| 2019-02-02 | 4.3 | A | 5.521E-02 | 3.0 | 0.4 | 0.44 | 0.08 | 282E+03 | 62 | 24 |
| | | B | 1.865E-02 | | | 2.02 | 0.08 | 5E+03 | | |
| 2019-02-02 | 8 | A | 4.781E-02 | 5.0 | 0.7 | 0.34 | 0.05 | 416E+03 | 30 | 10 |
| | | B | 9.550E-03 | | | 0.83 | 0.05 | 14E+03 | | |
| 2020-02-26 | 5 | A | 5.323E-02 | 4.3 | 0.6 | 0.57 | 0.05 | 166E+03 | 92 | 21 |
| | | B | 1.227E-02 | | | 2.60 | 0.05 | 2E+03 | | |

TABLE 5.9: J0900-0652

The FR does not have a constant value for the different epochs. The deviation between the first and latest epoch values at the C-band is 1.9 times the combined error. Moreover the SB ratio between the two components for all three available observations has a value much greater than 4.

The morphology observed in the latest epoch data seems to confirm a core+jet. Additionally the spectral indexes of the two components point to a much steeper spectrum for component B in agreement with the core+jet structure hypothesis. More specifically the two spectral indexes

were calculated to be -0.2 and -1.1 for component A and B respectively. This source can be discarded, as it is not a good gravitational lens candidate.

5.11 J0918+2650

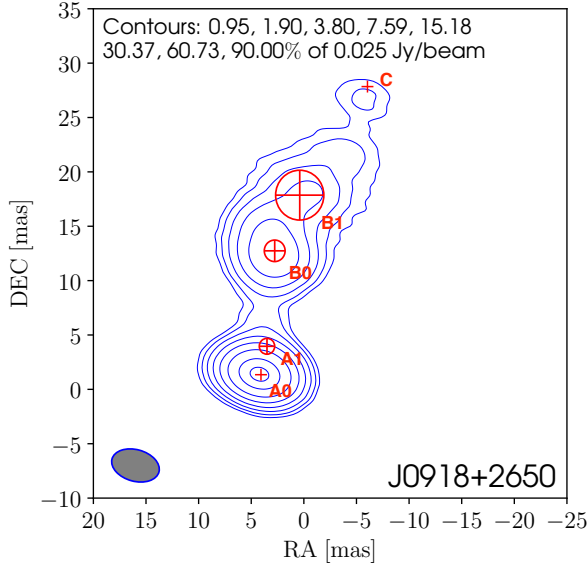


FIGURE 5.22: J0918+2650 EVN 5 GHz data

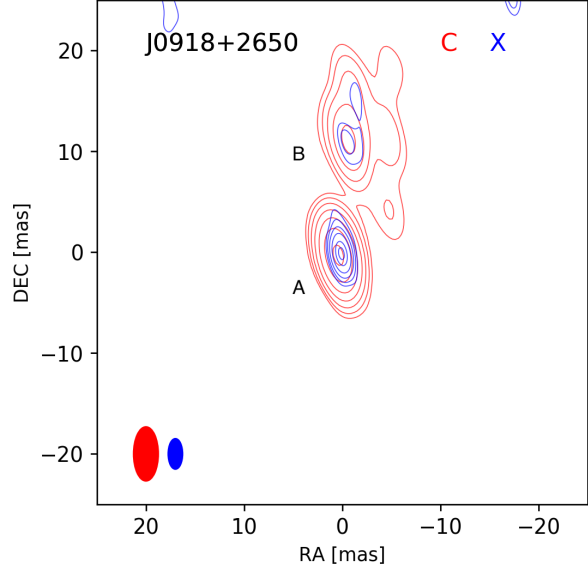


FIGURE 5.23: J0918+2650 Astrogro data at 4.3 GHz (C-band) and 8 GHz (X-band)

As with the previous source, the two structures are now clearly connected by a weaker extended emission.

| Epochs | Frequency (GHz) | Component | Flux (Jy) | Flux Ratio | Error | FWHM (milli-arcsec) | Error (milli-arcsec) | SB (Jy/arcsec ²) | SB Ratio | Error |
|------------|--------------------|-----------|--------------|---------------|-------|------------------------|-------------------------|---------------------------------|-------------|-------|
| 2015-10-25 | 4.3 | A | 2.458E-02 | 3.0 | 0.4 | 0.22 | 0.17 | 499E+03 | 40 | 65 |
| | | B | 8.295E-03 | | | 0.82 | 0.17 | 12E+03 | | |
| 2015-10-25 | 8 | A | 3.181E-02 | 4.3 | 0.6 | < 0.17 | 0.17 | >1081E+03 | >927 | |
| | | B | 7.457E-03 | | | 2.53 | 0.17 | 1E+03 | | |
| 2020-02-27 | 5 | A | 2.860E-02 | 1.6 | 0.2 | 1.46 | 0.12 | 13E+03 | 19 | 4 |
| | | B | 1.760E-02 | | | 4.99 | 0.12 | 1E+03 | | |

TABLE 5.10: J0918+2650

The FR does not seem to have a constant value for the different epochs. The deviation between the first and latest epoch values at C-band is 2.8 times the combined error. The SB ratio between the two components, in all three available observations has a value much greater than 4. It should be noted that the FWHM of component A in the 8 GHz observation was replaced with an upper bound equal to the minimum resolvable size. This was done because its initial value, as derived from the model-fitting process, was very small, corresponding to a delta function.

Moreover, the latest epoch data seems to confirm the core+jet structure, based on the morphology, the existence of an extended structure connecting the two components as well as the fact that component B is extending farther north. The spectral indexes of the two components show the spectrum of component B to be much steeper than that of component A in agreement with this assumption. The calculated values are 0.4 and -0.2 for component A and B respectively. This source does not seem to be a good gravitational lens candidate and can be discarded.

5.12 J1037+4335

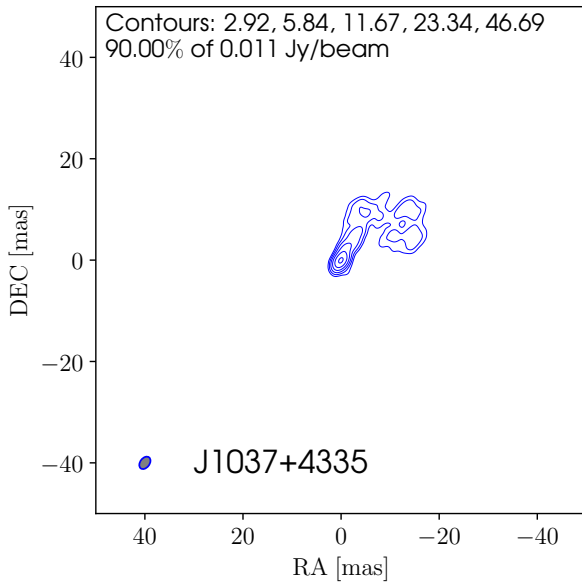


FIGURE 5.24: J1037+4335 EVN 5 GHz data

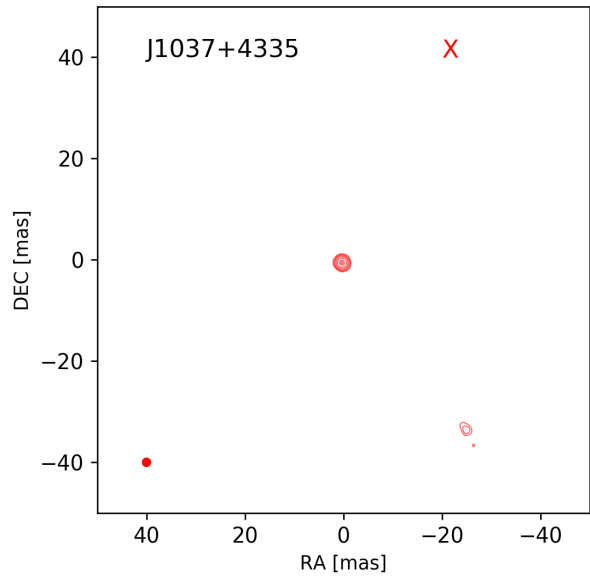


FIGURE 5.25: J1037+4335 Astrogro data at 8 GHz (X-band)

This source was initially discarded based on the SB criterion, using Astrogro data at 8 GHz. With the new high sensitivity observations we can notice that what we initially thought was a compact component is instead the core of an extended radio jet. The second component that was visible in the image from the Astrogro data is no longer shown in the new image from the EVN data. It is possible that this secondary component is an artifact. This source continues to be discarded as a lens candidate.

5.13 J1132+5100

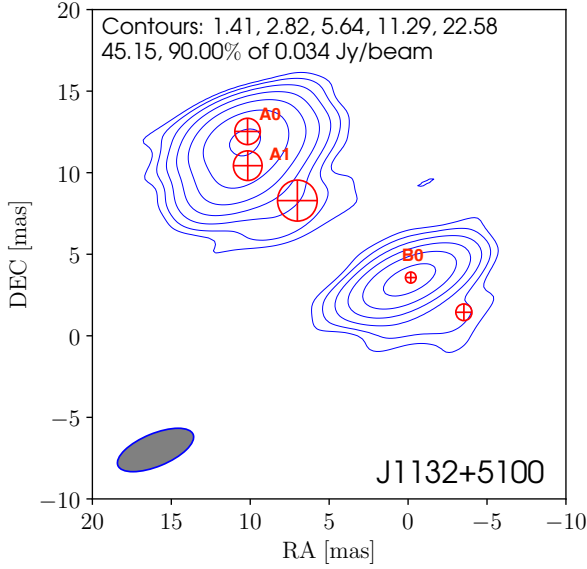


FIGURE 5.26: J1132+5100 EVN 5 GHz data

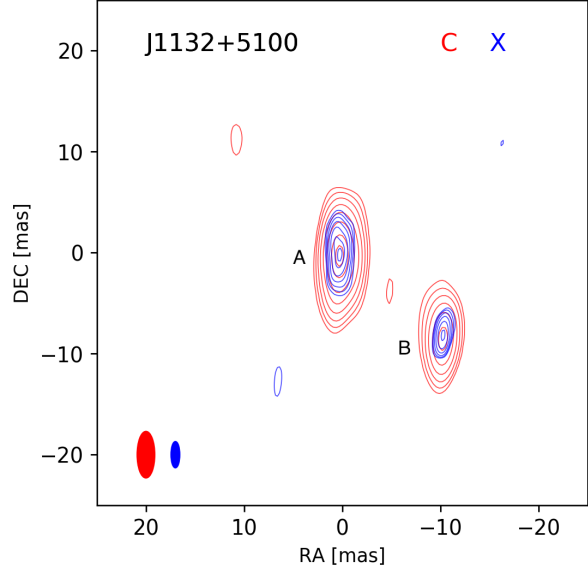


FIGURE 5.27: J1132+5100 Astrogéo data at 4.3 GHz (C-band) and 8 GHz (X-band)

| Epochs | Frequency (GHz) | Component | Flux (Jy) | Flux Ratio | Error | FWHM (milli-arcsec) | Error (milli-arcsec) | SB (Jy/arcsec ²) | SB Ratio | Error |
|------------|--------------------|-----------|--------------|---------------|-------|------------------------|-------------------------|---------------------------------|-------------|-------|
| 2013-04-22 | 4.3 | A | 8.002E-02 | 3.4 | 0.5 | 1.45 | 0.10 | 38E+03 | 1.2 | 0.4 |
| | | B | 2.367E-02 | | | 0.73 | 0.10 | 44E+03 | | |
| 2020-02-27 | 5 | A | 7.078E-02 | 2.8 | 0.4 | 3.81 | 0.11 | 5E+03 | 3.5 | 0.8 |
| | | B | 2.578E-02 | | | 1.23 | 0.11 | 17E+03 | | |

TABLE 5.11: J1132+5100

In the case of this source we also had one epoch at 8 GHz from Astrogéo that was subsequently not taken into account in the analysis. This is because the modelfit was deemed unreliable based on the large errorbars displayed by data.

The FR in the two epochs at C-band are separated by approximately one combined error. Additionally, the SB ratio in both observations has acceptable values. We should note here that for both available epochs the SB values of component B are constantly larger than those of component A. Therefore we calculated the SB ratio using the SB value of component B over that of component A.

The quantities of the last epoch were derived using a five-component model fitting using all components shown in Figure 5.26. We also proceeded to do the modelfit process using just three components (components A0, A1 and B0 as marked in the same Figure). In this case we get a slightly greater FR value compared to the case of the five-component model, equal to 3.0 and a

SB ratio equal to 6.4 ± 2.5 , that is still acceptable within error. We conclude that the available data are not sufficient to take this source out from the list of good lens candidates.

5.14 J1143+1834

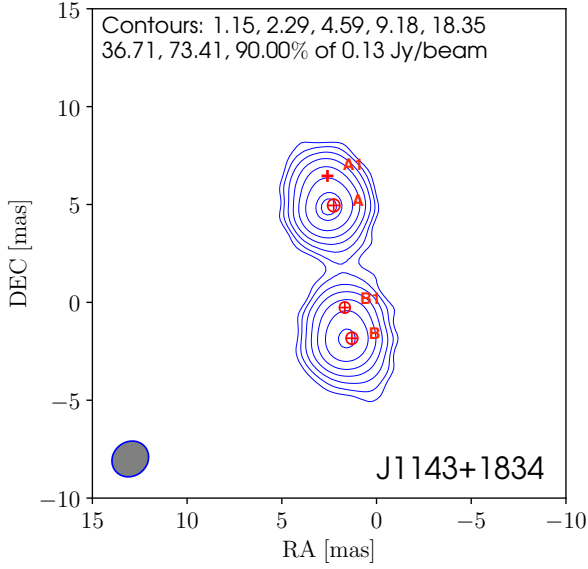


FIGURE 5.28: J1143+1834 EVN 5 GHz data

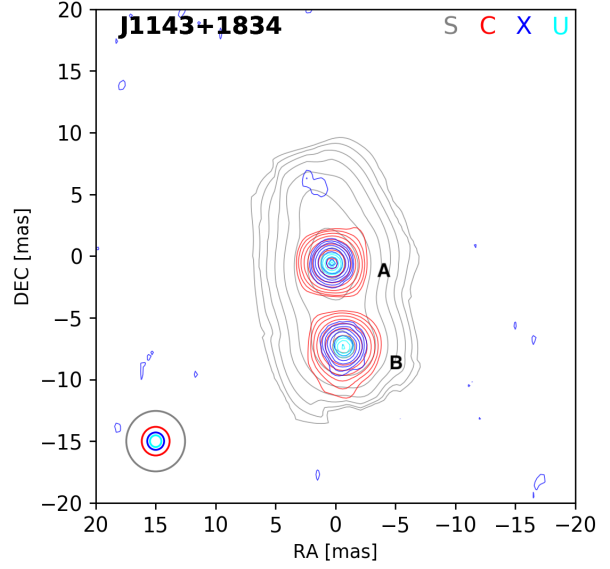


FIGURE 5.29: J1143+1834 Astrogio data at 2.3 GHz (S- band), 4.3 GHz (C-band), 8 GHz (X-band) and 15.1 GHz (U-band)

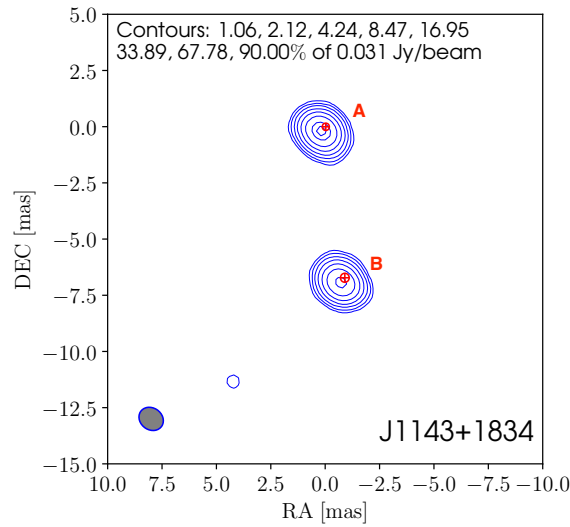


FIGURE 5.30: J1143+1834 EVN 22 GHz data

| Epochs | Frequency (GHz) | Component | Flux (Jy) | Flux Ratio | Error | FWHM (milli-arcsec) | Error (milli-arcsec) | SB (Jy/arcsec ²) | SB Ratio | Error |
|------------|--------------------|-----------|--------------|---------------|-------|------------------------|-------------------------|---------------------------------|-------------|-------|
| 2006-02-09 | 4.3 | A | 1.863E-01 | 1.2 | 0.2 | 0.31 | 0.07 | 1894E+03 | 3.6 | 1.9 |
| | | B | 1.604E-01 | | | 0.55 | 0.07 | 529E+03 | | |
| 2012-02-20 | 8 | A | 1.179E-01 | 1.2 | 0.2 | 0.43 | 0.04 | 643E+03 | 1.7 | 0.5 |
| | | B | 9.820E-02 | | | 0.51 | 0.04 | 381E+03 | | |
| 2015-01-23 | 8 | A | 8.007E-02 | 1.0 | 0.1 | 0.33 | 0.04 | 729E+03 | 2.2 | 0.8 |
| | | B | 7.742E-02 | | | 0.48 | 0.04 | 334E+03 | | |
| 2017-02-24 | 8 | A | 1.230E-01 | 1.0 | 0.1 | 0.34 | 0.04 | 1047E+03 | 1.4 | 0.4 |
| | | B | 1.167E-01 | | | 0.39 | 0.04 | 771E+03 | | |
| 2008-05-15 | 15.1 | A | 5.119E-02 | 1.2 | 0.2 | 0.21 | 0.06 | 1135E+03 | 1.7 | 1.3 |
| | | B | 4.463E-02 | | | 0.26 | 0.06 | 660E+03 | | |
| 2020-02-26 | 5 | A | 1.726E-01 | 1.1 | 0.2 | 0.65 | 0.07 | 411E+03 | 1.9 | 0.6 |
| | | B | 1.545E-01 | | | 0.84 | 0.07 | 219E+03 | | |
| 2020-03-04 | 22 | A | 3.363E-02 | 1.2 | 0.2 | 0.33 | 0.03 | 315E+03 | 1.8 | 0.6 |
| | | B | 2.784E-02 | | | 0.40 | 0.03 | 172E+03 | | |

TABLE 5.12: J1143+1834

The FR has very similar values for all the different epochs. The values of the FR for the observations at 4.3 GHz and 5 GHz were calculated close to 0.2 times the combined error. Moreover, the SB ratio between the two components, in every available epoch has a value lower than 4. The available data suggests that the SB criterion is fulfilled in every observational epoch.

We also calculated the spectral index of the two components using the EVN data at 5 and 22 GHz and we found values of -1.1 and -1.2 for component A and B respectively. The two components have similar spectral indexes as expected in cases of gravitational lens systems.

Finally, we used the positions of the two components and we calculated the distance between them. For the new EVN observations at 5 GHz this distance was found equal to 6.85 ± 0.07 mas, while at 22 GHz we obtained 6.77 ± 0.03 mas. Similarly, for the oldest available epoch (2006-02-09 at 4.3 GHz) this same distance was found to be equal to 6.84 ± 0.07 mas. We can conclude that all the calculated values are in agreement within errors, meaning that the distance between the components does not exhibit any major change, either in time or between frequencies.

This is a very interesting source, since, despite the many available epochs and different datasets, can still be considered a millilens candidate.

5.15 J1306+0341

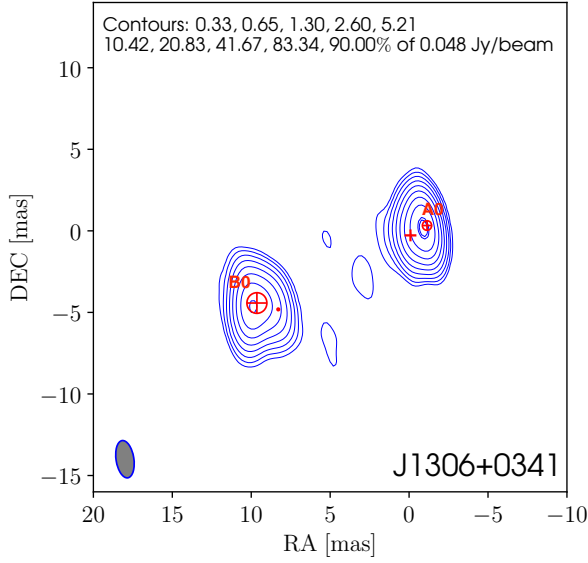


FIGURE 5.31: J1306+0341 EVN 5 GHz data

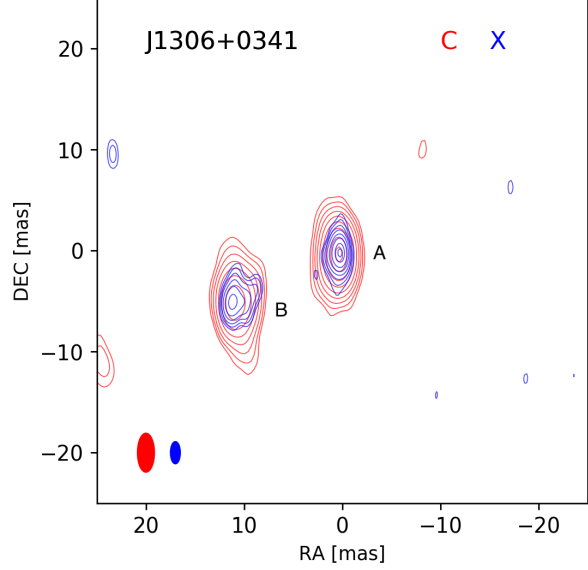


FIGURE 5.32: J1306+0341 Astrogro data at 4.3 GHz (C-band) and 8 GHz (X-band)

| Epochs | Frequency (GHz) | Component | Flux (Jy) | Flux Ratio | Error | FWHM (milli-arcsec) | Error (milli-arcsec) | SB (Jy/arcsec ²) | SB Ratio | Error |
|------------|--------------------|-----------|--------------|---------------|-------|------------------------|-------------------------|---------------------------------|-------------|-------|
| 2014-01-27 | 4.3 | A | 9.757E-02 | 1.6 | 0.2 | 0.90 | 0.06 | 122E+03 | 4.8 | 1.0 |
| | | B | 6.028E-02 | | | 1.54 | 0.06 | 26E+03 | | |
| 2014-01-27 | 8 | A | 4.784E-02 | 1.6 | 0.2 | 0.65 | 0.05 | 113E+03 | 8.4 | 1.8 |
| | | B | 2.975E-02 | | | 1.49 | 0.05 | 13E+03 | | |
| 2020-02-26 | 5 | A | 6.567E-02 | 1.6 | 0.2 | 0.59 | 0.03 | 191E+03 | 7.3 | 1.3 |
| | | B | 4.227E-02 | | | 1.27 | 0.03 | 26E+03 | | |

TABLE 5.13: J1306+0341

The FR at the two observational epochs at 4.3 and 5 GHz has a constant value. Despite the preservation of the FR between the components, the SB ratio value is found larger than 4 at all available observations. This source does not follow the SB criterion.

The physical quantities computed in the last epoch are the result of a four-component model fit, where we have considered all components shown in Figure 5.32. We also obtain the same quantities for a two component modelfit, using only components A0 and B0 and the resulting FR was found to be equal to 1.5, with a deviation of 0.3 times the error from the first epoch value. Also, for the two components modelfit, the SB ratio is over 4, more specifically 7.1. In conclusion, this source is not a good lens candidate.

5.16 J1344-1739

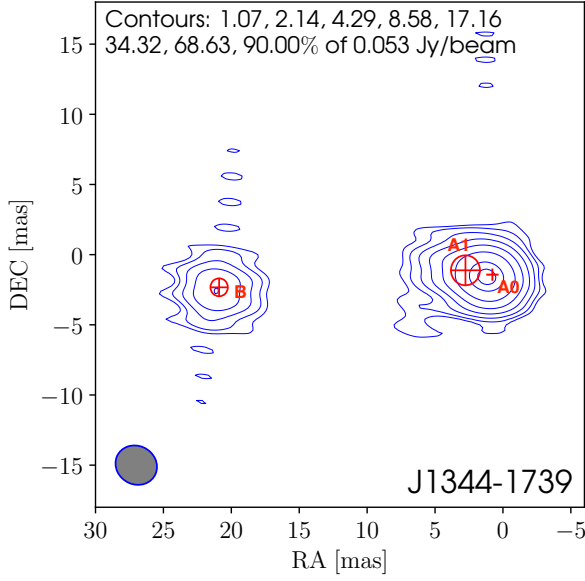


FIGURE 5.33: J1344-1739 EVN 5 GHz data

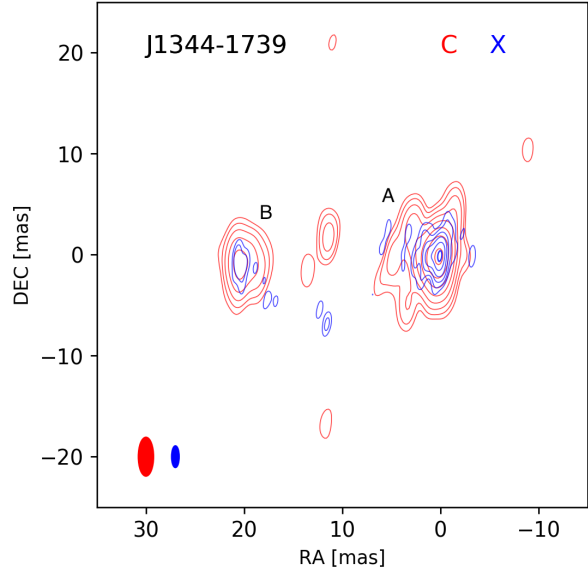


FIGURE 5.34: J1344-1739 Astrogro data at 4.3 GHz (C-band) and 8 GHz (X-band)

| Epochs | Frequency (GHz) | Component | Flux (Jy) | Flux Ratio | Error | FWHM (milli-arcsec) | Error (milli-arcsec) | SB (Jy/arcsec ²) | SB Ratio | Error |
|------------|--------------------|-----------|--------------|---------------|-------|------------------------|-------------------------|---------------------------------|-------------|-------|
| 2014-01-27 | 4.3 | A | 9.263E-02 | 5.2 | 0.7 | 1.67 | 0.06 | 33E+03 | 10.0 | 1.7 |
| | | B | 1.790E-02 | | | 2.31 | 0.06 | 3E+03 | | |
| 2014-01-27 | 8 | A | 5.053E-02 | 8.0 | 1.2 | 1.18 | 0.06 | 36E+03 | 10.2 | 2.0 |
| | | B | 6.341E-03 | | | 1.34 | 0.06 | 4E+03 | | |
| 2020-02-27 | 5 | A | 6.282E-02 | 5.8 | 0.8 | 2.14 | 0.15 | 14E+03 | 2.1 | 0.6 |
| | | B | 1.091E-02 | | | 1.28 | 0.15 | 7E+03 | | |

TABLE 5.14: J1344-1739

The FR in the new EVN 5 GHz image and in the Astrogro 4.3 GHz image are in agreement within errors. However, the two observations from the Astrogro dataset have SB ratio values close to 10, that are way over the acceptable upper bound we have set. This source can be discarded based on the SB test.

Chapter 6

Conclusion

In this work we focused on 16 sources, of which 9 were included in the 40 best candidates list presented in the SMILE pilot study (Casadio et al. 2021). We used new EVN data at 5 and 22 GHz to create the images of these sources and analyse some of the physical quantities of the compact components forming these sources' images. We set a number of criteria that these physical quantities should adhere to in order for the sources to still be considered possible gravitational lenses. Older Astrogéo data were also included in our analysis to compare the data from different epochs and test physical quantities that we expect to be preserved in time, like the flux density ratio between the same components at the same observing frequency. Among all sources, three seem to pass all the posed tests: J0237+1116, J1132+5100 and J1143+1834. The rest of sources instead can be discarded as possible milli-lens candidates. Among the confirmed lens candidates, J1143+1834 is a standout source since it is the source with the most extended dataset (6 observational epochs and 4 different frequency bands) and it passes all tests with great accuracy. For this reason it can be considered the most promising of the lens candidates studied in this work and it will be studied further in a future work. For all sources that are still judged as possible lens candidates, further multi-frequency VLBI observations could be crucial for confirming the real nature of these objects. Additionally, the study of the optical counterparts could be fundamental to discriminate between the various scenarios concerning the nature of these sources. Finally, even in the case where we reject an object as a gravitational lens candidate, this source can still be investigated as a CSO or a SBBH candidate. Both of these alternative cases are of high scientific interest for further studies.

Bibliography

- Abdo, A. A., Ackermann, M., Ajello, M., et al. 2011, *The Astrophysical Journal*, 736, 131
- Browne, I. W. A., Wilkinson, P. N., Jackson, N. J. F., et al. 2003, *Monthly Notices of the Royal Astronomical Society*, 341, 13
- Bullock, J. S. & Boylan-Kolchin, M. 2017, *Annual Review of Astronomy and Astrophysics*, 55, 343
- Casadio, C. 2016, PhD thesis, Institute of Astrophysics of Andalusia
- Casadio, C., Blinov, D., Readhead, A. C. S., et al. 2021, *Monthly Notices of the Royal Astronomical Society: Letters*, 507, L6
- Casadio, C., Marscher, A. P., Jorstad, S. G., et al. 2019, *Astronomy & Astrophysics*, 622, A158
- Del Popolo, A. 2002, *Dark matter, density perturbations and structure formation*
- Frey, S., Gabányi, K. É., & An, T. 2022, *Symmetry*, 14, 321
- Gomez, J. L., Marti, J. M. A., Marscher, A. P., Ibanez, J. M. A., & Marcaide, J. M. 1995, , 449, L19
- Hezaveh, Y. D., Dalal, N., Marrone, D. P., et al. 2016, *The Astrophysical Journal*, 823, 37
- Högbom, J. A. 1974, , 15, 417
- Kiehlmann, S., Lister, M. L., Readhead, A. C. S., et al. 2023a, *Towards a Comprehensive Catalog of Bona Fide Compact Symmetric Objects*
- Kiehlmann, S., Readhead, A. C. S., O'Neill, S., et al. 2023b, *Compact Symmetric Objects: A Distinct Population of Jetted Active Galaxies*

- Konigl, A. 1981, , 243, 700
- Lobanov, A. P. 2005, Resolution limits in astronomical images
- Longair, M. S. 2011, High Energy Astrophysics
- Loudas, N., Pavlidou, V., Casadio, C., & Tassis, K. 2022, Discriminating power of milli-lensing observations for dark matter models
- Marscher, A. P. 2008, in Astronomical Society of the Pacific Conference Series, Vol. 386, Extragalactic Jets: Theory and Observation from Radio to Gamma Ray, ed. T. A. Rector & D. S. De Young, 437
- Nair, D. G., Lobanov, A. P., Krichbaum, T. P., et al. 2019, , 622, A92
- Orienti, M. & Dallacasa, D. 2020, Monthly Notices of the Royal Astronomical Society, 499, 1340
- Paduroiu, S., Revaz, Y., & Pfenniger, D. 2015, Structure formation in warm dark matter cosmologies: Top-Bottom Upside-Down
- Popolo, A. D. & Delliou, M. L. 2017, Galaxies, 5, 17
- Readhead, A. C. S., Ravi, V., Blandford, R. D., et al. 2023, The Evolution of Compact Symmetric Objects – A Possible Connection with Tidal Disruption Events
- Schwab, F. R. & Cotton, W. D. 1983, , 88, 688
- Taylor, G. B., Rodriguez, C., Zavala, R. T., et al. 2006, Proceedings of the International Astronomical Union, 2, 269–272
- Vegetti, S., Lagattuta, D. J., McKean, J. P., et al. 2012, Nature, 481, 341
- Viel, M., Lesgourgues, J., Haehnelt, M. G., Matarrese, S., & Riotto, A. 2005, Physical Review D, 71
- Voggel, K. T., Seth, A. C., Baumgardt, H., et al. 2022, Astronomy & Astrophysics, 658, A152
- Weinberg, D. H., Bullock, J. S., Governato, F., de Naray, R. K., & Peter, A. H. G. 2015, Proceedings of the National Academy of Sciences, 112, 12249
- Wilkinson, P. N., Henstock, D. R., Browne, I. W. A., et al. 2001, Physical Review Letters, 86, 584